DIGITALLY CONTROLLED MICROWAVE COMPONENTS FOR HIGH-POWER RADAR SYSTEMS

TAREK DJEDDI

A THESIS
IN
THE DEPARTMENT
OF
ELECTRICAL AND COMPUTER ENGINEERING

PRESENTED IN PARTIAL FULFILLEMENT OF THE
REQUIREMENTS
FOR THE DEGREE OF MASTER OF APPLIED SCIENCES
CONCORDIA UNIVERSITY
MONTREAL, QUEBEC CANADA

JULY 2018

CONCORDIA UNIVERSITY
SCHOOL OF GRADUATE STUDIES

This is to certify that the thesis prepared

By: Tarek Djeddi

Entitled: Digitally Controlled Microwave Components For High-Power Radar Systems

and submitted in partial fulfillment of the requirements for the degree of

Master of Applied Science

complies with the regulations of this University and meets the accepted standards with respect to originality and quality.

Signed by the Final Examining Committee:

_____ Chair
Dr. D. Qiu

_____ Examiner, External To the Program
Dr. J. Bentahar (CIISE)

_____ Examiner
Dr. Yousef Shayan

_____ Supervisor
Dr. Walaa Hamouda

Approved by: _____
Dr. W. E. Lynch, Chair
Department of Electrical and Computer Engineering

_____ 20____

_____
Dr. Amir Asif, Dean
Faculty of Engineering and Computer Science

Abstract

Digitally Controlled Microwave Components For High-Power Radar Systems

TAREK DJEDDI

Radar Systems are among the most widely used communication systems. They are used in both military and civilian applications such as: Remote sensing, Microwave Sounder (MWR), Ship Navigation, and Air Traffic Control (ATC). Radar systems use high power electromagnetic signals to detect and locate faraway objects such as aircrafts or ships. The development of radar started in the $1930s$, before and during the Second World War, however it is still an important area of research with its critical role in various applications.

Typically, radar systems require high-power to cover large areas. Such high power cannot be derived from one source. Therefore, multiple power sources are combined together to achieve such high-power, where these sources must be synchronized and in-phase. In the normal operation of a traditional power combining network, the internal matching of the network is the most important design factor, so that the power sources will be combined without any significant losses. However, in case of failure of any source before the combining stage, the power of the working sources will be reflected and dissipated into a protection circuit causing huge losses and degradation in the overall system performance.

In theory, it is impossible for any three-port passive networks (such as power combiners) to satisfy three conditions: losslesssness, internal matching, and the reciprocity. The power combining is usually made out of conducting linear material to satisfy both the reciprocity and the losslessness conditions. Hence, the failure of one source at the combiner port leads to reflection as the network theoretically cannot be internally matched. To overcome this limitation, the power combining system must deploy active components to avoid the mismatch situations.

In this thesis, we propose a system which improves the performance of power combining networks by detecting the failure events of the malfunctioning source and directs the properly-functioning source to the output by the aid of electrically controlled switches.

The proposed system uses directional couplers to extract a power sample from the signal passing through each branch. We build and test the controlling subsystem where all the required elements are integrated up to the proposed design. Moreover, we propose a novel Band-Pass Filter (BPF) structure using coupled structure resonators to reject the out-band and reduce the noise power as a pre-filtering stage to the energy detection. Also, energy detection technique is used to identify which power source is still in operation. Finally, we provide closed-form mathematical expressions for the performance of the proposed energy detector in terms of the probability of false alarm and detection.

Acknowledgments

I would like to express my deepest gratitude to Prof. Walaa Hamouda for giving me the opportunity to do my thesis program under his supervision by his guidance during my program, his encouragements, and his help for choosing the suitable courses. Also, I would like to thank him for his support and understanding..

I would like to express special thanks to Dr. Mahmoud Elsaadany for his guidance and for his support in every stage of my project.

Moreover, I am grateful to Dr. Shoukry Shams for being patient with me and for teaching me how to design and manufacture the microwave filter. Last but not least, I am fully indebted to my parents and my brothers for their encouragements and moral support.

Contents

List of Figures

List of Tables

List of Symbols

G	The antenna gain
G_t	Transmit antenna gain
G_r	Receive antenna gain
W_t	Transmitted power
W_r	Received power
P_d	Probability of detection
P_{fa}	Probability of false alarm
P_m	Probability of miss detection
H_0	Hypotheses 0
H_1	Hypotheses 1
$y(t)$	Received signal
f_c	The cut-off frequency
f_{min}	The minimum frequency
f_{max}	The maximum frequency
f_0	The central frequency
C	Capacitor
L	Inductor
N	Order of the filter
w_c	The reference angular frequency
βl_k	the electrical length of each element value k
Z_0	Line impedance
Z_h	The highest practical line impedance
Z_l	The lowest practical line impedance
τ	The transmission delay
θ	the electrical length in radian

λ	Wavelength
P_{IN}	The input power of the RF signal
$n(t)$	Noise waveform
$s(t)$	Signal waveform
T	Observation time interval
W	Bandwidth
$TW = u$	Time bandwidth product
V	The test statistic (decision statistic)
a_i	Noise sample value
i	Number of samples
σ^2	Variance
N_{02}	Two-sided noise power density spectrum
$R(\tau)$	Autocorrelation function
$\phi_i(t)$	Eigenfunctions
g_i	Eigenvalues
V'	Normalized test statistic
b_i	Normalized noise sample value
α_i	Signal sample value
β_i	Normalized signal sample value
$y^2(t)$	The energy of $y(t)$
λ	Noncentrality parameter
E_s	Signal energy
$n_c(t)$	The in-phase component of the n(t)
$n_s(t)$	The quadrature component of the n(t)
$n_c^2(t)$	The energy of $n_c(t)$
$n_s^2(t)$	The energy of $n_s(t)$
a_{ci}	The noise sample value of $n_c(t)$
a_{si}	The noise sample value of $n_s(t)$
bci	The normalized noise sample value of a_{ci}
bsi	The normalized noise sample value of a_{si}
β_{ci}	The normalized signal sample value of s_{ci}
β_{si}	The normalized signal sample value of s_{si}

$V_T^{'}$	Threshold
X_k^2	Chi-square distribution with k degrees of freedom
$X_k^2(\lambda)$	Noncentral chi-square distribution with k degrees of freedom and noncentrality parameter λ
D	Modified number of degrees of freedom
G	Threshold divisor
$Env^2[n(t)]$	Squared envelope of n(t)
$Env^2[s(t)]$	Squared envelope of s(t)
γ	Signal-to-noise ratio
$f(.)$	Probability density function
$\Gamma(.)$	Gamma function
$I_n(.)$	The nth-order modified Bessel function of the first kind
$\Gamma(.,.)$	Incomplete gamma function
$F(.)$	Cumulative distribution function
$Q_M(a,b)$	Generalized Marcum Q-function
$\overline{P_d}$	Average probability of detection

List of Acronyms

RF	Radio Frequency
VSWR	Voltage Standing Wave Ratio
ED	Energy Detection
BPF	Band-pass Filter
ROC	Receiver Operating Characteristic
PCB	Printed Circuit Board
AWGN	Additive white Gaussian noise
UHF	Ultra-High Frequency
MF	Microwave Frequency
CW	Continues Wave
PR	Pulsed Radar
IF	Intermediate Frequency
PRF	Pulse Repetition Frequency
PDR	Pulse Doppler Radar
MTI	Moving Target Indicator Radar
COHO	Coherent Oscillator
STALO	Stable Local Oscillator
RPC	Resistive Power Combiner
HPC	Hybrid Power Combiner
WC	Wilkinson Combiner
UWB	Ultra-Wide-Band
CPW	Coplanar Waveguide
RW	Rectangular Waveguide
MMICs	Monolithic Microwave Integrated Circuits
MM wave	Millimeter Wave

SNR	Signal-to-Noise Ratio
DSP	Digital Signal Processor
LPF	Low Pass Filter
HPF	High Pass Filter
ADS	Advanced Design System
TINA	Toolkit for Interactive Network Analysis
CST	Computer Simulation Technology
SMA	Sub-Miniature version A
SR flip-flop	Set-Reset flip-flop
VIN-	Input Voltage
VCAL	Threshold Calibration
IDE	Arduino Software
DW	Double-ridge Waveguide
PDF	Probability Density Function
CDF	Cumulative Distribution Function

Chapter 1

Introduction

Radar uses radio waves to determine the presence, the velocity, and the angular position of an object. It radiates electromagnetic energy into space and detects the reflected or echo signal coming from objects. The receiving antenna transmits the energy to a receiver for extracting the information about the object such as: the location and velocity. In detecting a moving target, the frequency shift of the reflected signal due to the doppler effect is used to calculate the velocity and distinguish a moving target from stationary targets [1]. The operating high gain and the wide bandwidth of the antennas are critical for the quality of the resolution for the radar systems. Thus, there is a need for ultra wide band antennas [2]-[5].

There are three basic methods for implementing radar systems, namely: Quasi-monostatic, Monostatic, and Bistatic [6], [7]. Quasi-monostatic method is used when there is a small separation between the transmitter and the receiver, whereas monostatic method is used when the transmitter and the receiver units share the same antenna. The bistatic method is used when the transmitter and the receiver are separated away from each other as shown in Figure 1.1. In Fig. 1.1, G is the antenna gain, G_t is the transmit antenna gain, G_r is the receive antenna gain, W_t and W_r are the transmitted and received powers respectively. It is worth mentioning that in some radar applications, the antenna is designed to have a specific polarization or to operate in multi bands for overall better performance [8]-[11].

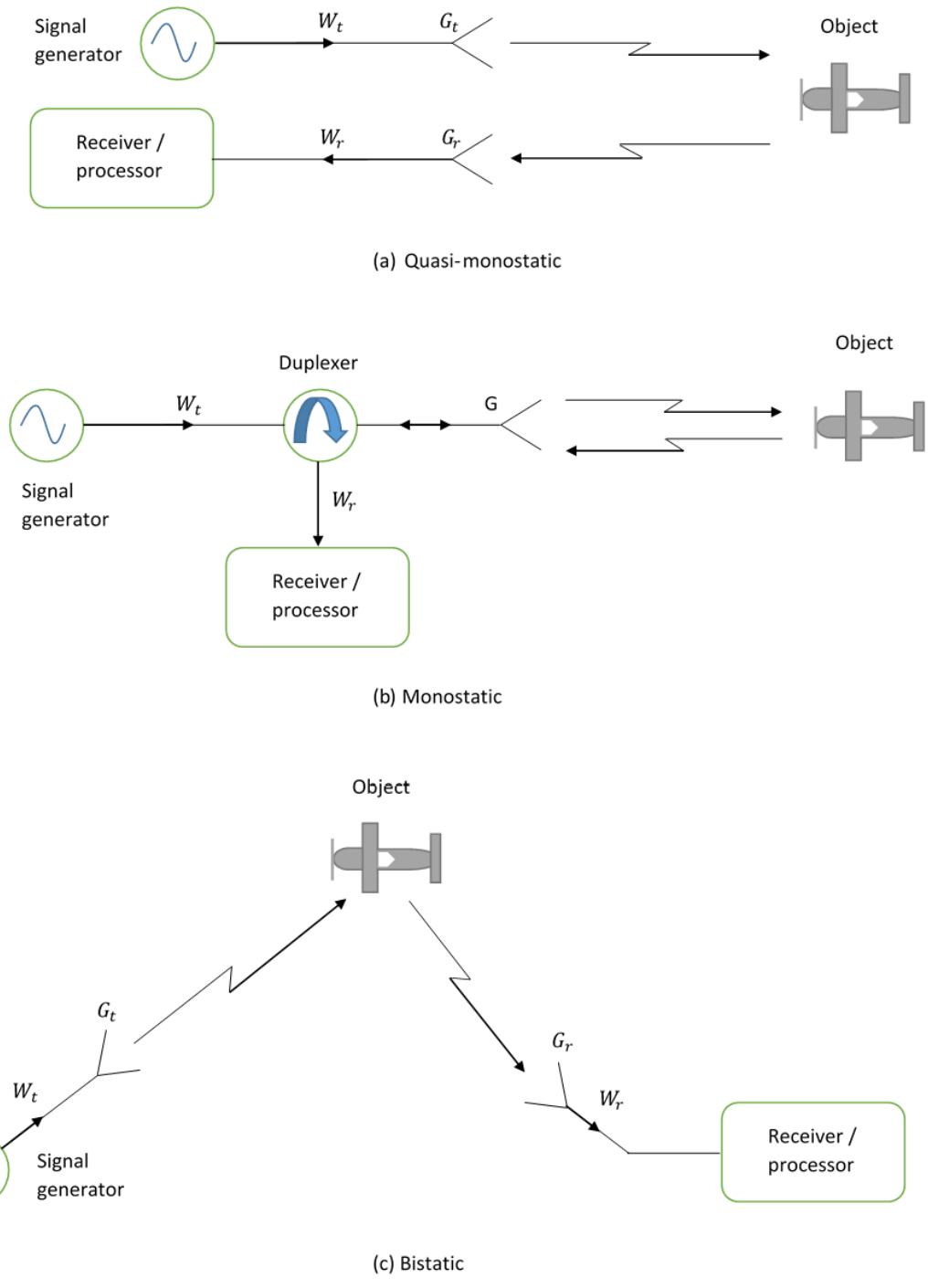

Figure 1.1: Basic methods for implementing radar systems

1.1 Power Combiners

Power combiners are used to combine several power signals (input signals) into a common power signal (single output) while maintaining the same characteristic impedance of the input signals. Moreover, they are used widely in Radio Frequency (RF) applications like: power amplifiers, and antennas. The advantages of power combiners are: low insertion loss, excellent phase balance, high power handling, good isolation levels, and low Voltage Standing Wave Ratio (VSWR). Hybrid combiners are commonly used in combining the power of power amplifiers due to their small size [12]-[15].
There are several methods for power combining such as: Circuit-level Combining, Spatial Power Combining, Radial Power Combining, and magic Tee networks [16], [17].

1.2 Energy Detection Technique

In this thesis, we use the Energy Detection (ED) technique in the implementation of the proposed digital system. Energy detection technique simply calculates the energy of the signal. The presence or the absence of the signal in the band can be detected by comparing the decision statistic with a threshold. Energy detection technique can be used in both frequency and time domain (direct and indirect techniques). In fact, energy detection technique is the most popular technique in the non cooperative sensing techniques due to its reliable performance and simple implementation. However, it requires some sensing time to achieve the suitable probability of detection (P_d) and the probability of false alarm (P_{fa}) [18]. A flowchart of the conventional energy detection technique is illustrated in Figure 1.2 [19].

1.3 Motivation

Theoretically, it is impossible for any three port passive network to satisfy three conditions: losslessness, reciprocity and reflection free [20]. For example, isolated power combining subsystems which are widely used in radar systems, a lossless subsystem and the internal matching at all ports are mandatory conditions. However, this comes at the cost of the reciprocity condition. A possible compensation for such cost can be achieved by using an external controller circuit.

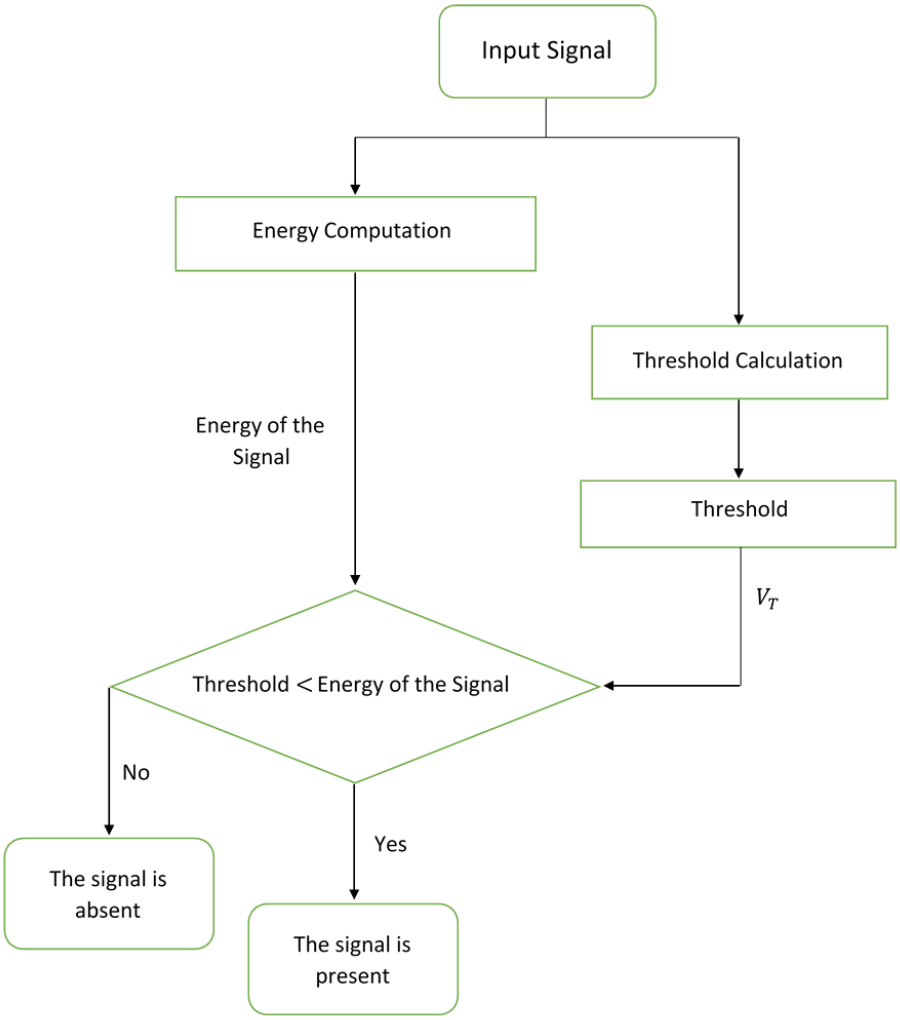

Figure 1.2: Conventional energy detection technique

In most of the cases, the maximum power available from a single power source is not sufficient for high power radar systems. One common solution used in radar systems is to combine the power from two synchronized sources with the aid of protection circuits. A traditional choice of protection circuit consists of two isolators in front of the power amplifiers. On the other hand, in case of failure operation of one of the branches, the power of the other branch is dissipated into the load of the isolator, resulting in reducing the efficiency of the radar system.

1.4 Summary of Contributions

We propose a system which improves the efficiency of power combining networks by detecting the failure events of the malfunctioning source. Then we implement a system that directs the working power source to the output by using electrically controlled switches. These electrically controlled switches are controlled by a controlling circuit. Specifically, the proposed system uses directional couplers to extract a power sample from the signal passing through each of the two branches. We build and test this controlling subsystem, where all the required elements are integrated in the proposed system. Moreover, we propose a very compact Band-pass Filter (BPF) structure using coupled structure resonators to reject the undesired signals and reduce the noise power as a pre-filtering stage to the energy detection. We propose using energy detection technique to detect which power source is still in operation. Finally, we provide closed-form mathematical expressions for the performance of the proposed energy detector in terms of the probability of false alarm and detection by plotting Receiver Operating Characteristic (ROC) curves.

1.5 Thesis Overview

The thesis is arranged as follows, chapter 2 introduces the relevant literature review of the topics covered in the thesis.
In chapter 3, we firstly present the traditional power combining network in the normal operation and in the case of failure. We show that the proposed system is able to improve the efficiency of the traditional power combining network in the case of failure.
In chapter 4, we present the traditional way for designing a band-pass filter. We use coupled structure technique in order to have a very compact size for the proposed band-pass filter. We propose adding a stepped transform to the input and output coupling stages to enhance the overall matching. Also, the performance of the out-band rejection improves by adding a symmetric coupled-line resonator. Our fabricated filter has a very compact size.
In chapter 5, we present the circuit implementation of the proposed system. We highlight different Printed Circuit Boards (PCBs) applying the energy detection technique.
In chapter 6, we present the hypotheses testing of the energy detection. We illustrate the detection in base-band and band-pass processes. we show the computation of the probability of detection and probability of false alarm over Additive white Gaussian noise (AWGN) and Rayleigh channels. Also, we present the performance of the energy detection over

AWGN and Rayleigh channels by plotting the receiver operating characteristic curves.
In chapter 7, we present the conclusion of the thesis and suggest some potential ideas for the future work.

Chapter 2

Background

2.1 Radar Systems

The story behind the concept of radar goes back to the late 19th century when Heinrich Hertz decided to verify the theoretical Maxwell's equations of electromagnetism in an experimental environment. Maxwell's equations proved that radio waves do reflect from metallic objects and refract when they hit a dielectric medium, which proved that radio waves do behave like optical light waves. In 1888, Hertz succeeded in demonstrating Maxwell's theory by an experiment in which a radio wave at 455 MHz is used [21]-[23]. In the 20th century, application of radar systems in many real world cases got the attention of scientists and researchers. This led to the development of the first use of radar systems in the military field in the 1930s which was able to detect aircrafts from the radio echos. Another application of radar systems was demonstrated by Christian Hulsmeyer in ships in order to detect objects in foggy environments to avoid collisions [6], [21]-[23].

Radar which stands for Radio Detection And Ranging systems is an electromagnetic signal used to find the location and the distance (range) of an object from the position of the radar. Radar radiates energy into air (space) and receives the reflected or echo signal coming from the target object. It operates at Ultra-High Frequency (UHF) and Microwave Frequency (MF). The antenna of the radar receives the reflected signal which is then passed to the receiver to determine the geographical position and velocity of the target [7], [24]. Figure 2.1 illustrates the main five components of any basic radar system [25], [26]:

1-Transmitter: Produces radio waves that are transmitted into space by the antenna.

2-Antenna: acts as a medium between the radar and the space, where it transmits radio

waves coming from the transmitter via duplexer into the space. It also receives the reflected signal or echo signal and passes it to the receiver through duplexer to extract the information about the object.

3-Duplexer: acts like a switch between the antenna and the transmitter or the receiver modes. When the duplexer is connected between the transmitter and antenna, the duplexer switch off the connection between the antenna and the receiver and vice versa.

4-Receiver: receives the echo signal or reflected signal coming from the antenna, demodulates and processes the echo signal to display.

5-Threshold Decision: compares the received signal with a threshold to detect the presence or the absence of any object.

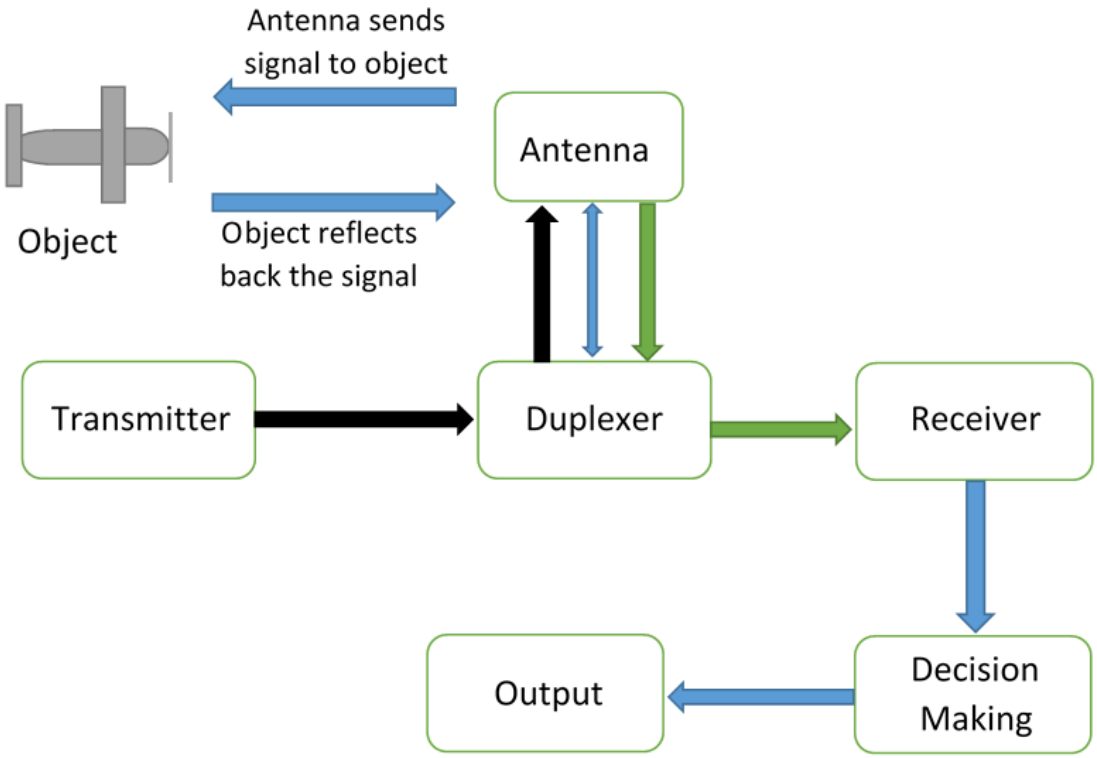

Figure 2.1: Basic Radar System

The range between the radar and the target can be obtained by computing the propagation time of the reflected signal. While finding the direction of arrival of the reflected energy, the angular position of the target can be known. Alternatively, the angular position can be determined by using narrow antenna beams (directive antenna) to sense the angle of arrival.

Doppler effect (Doppler shift) is used to measure the range and the location of a moving object, it is the change in the frequency of radio waves due to the movement of the object [1], [6], [25].

There are two types of Radar, namely: Continuous Wave (CW) radar and Pulsed Radar (PR). Continuous wave radar measures the rate of change in distance to the target which is used to determine the velocity of the target by measuring the doppler shift of the reflected signal. Figure 2.2 gives block diagram of continuous wave radar.

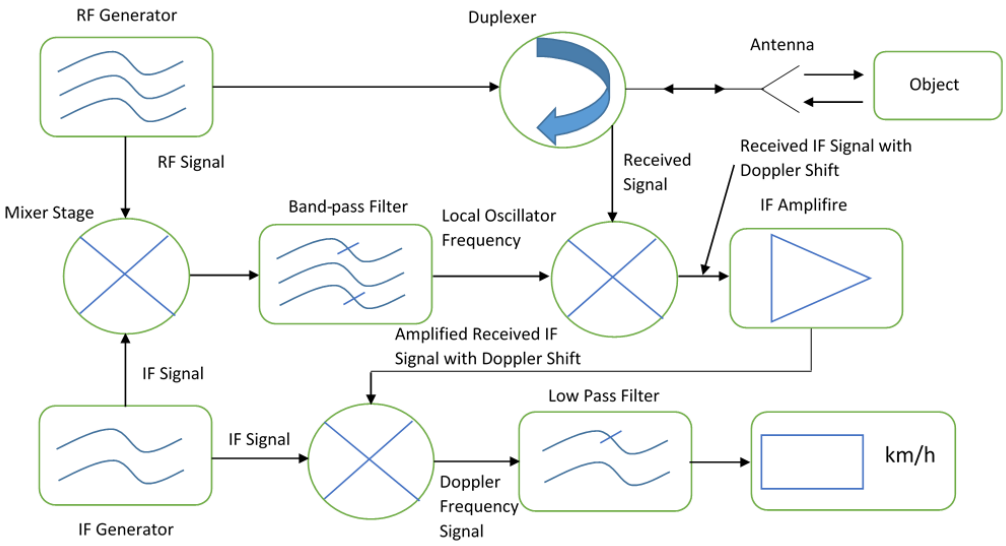

Figure 2.2: Block Diagram of Continuous Wave Radar.

The local oscillator frequency is generated by mixing the RF signal with the Intermediate Frequency (IF) signal in a mixer stage followed by a band-pass filter. The RF signal is transmitted into space by the antenna while the received signal from the antenna is the RF signal with the doppler shift frequency. Moreover, the IF signal with the doppler shift frequency is generated by mixing the received signal with the local oscillator frequency in the second mixing stage. The IF signal is amplified and goes to a third mixture stage which will be mixed with the IF signal to get the doppler frequency signal. It is fed to a low pass filter to measure the velocity of the target [1], [6], [25], [27].

Pulsed radar transmits high frequency and high power pulses to the space and waits for the reflected signal coming from the object before transmitting another pulse. The range and the resolution of the radar are affected by the Pulse Repetition Frequency (PRF).

There are two types of pulsed radar, namely: Pulse Doppler Radar (PDR) and Moving Target Indicator Radar (MTI) [1], [6], [25]. Pulse doppler radar avoids doppler ambiguities (blind speeds) by transmitting high pulse repetition frequency to measure the velocity of the target. Doppler ambiguities happen when the pulse repetition frequency is less than the doppler frequency. But, range ambiguous measurements (second-time-around echoes) affect the performance of pulse doppler radars since they operate by transmitting high pulse repetition frequency [28]. Figure 2.3 shows block diagram of pulsed doppler radar. The transmitted signal and the received reflected signal are mixed by a detector (mixer stage) and passed to a doppler filter to remove the undesired signals to obtain the doppler shift to measure the velocity of the target [1], [6], [25].

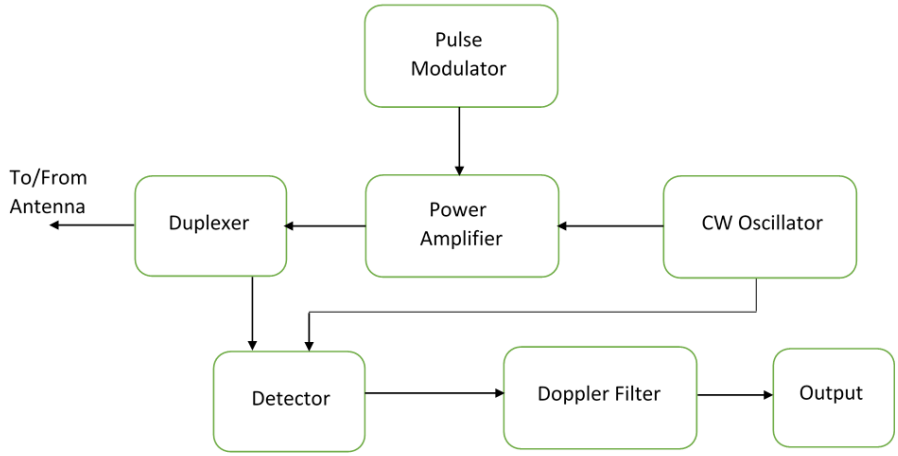

Figure 2.3: Block Diagram of Pulsed Doppler Radar.

Moving target indicator (MTI) radar operates by transmitting low pulse repetition frequency, so it can not avert the doppler ambiguities, while range ambiguous measurements do not affect the performance of moving target indicator radar.

Figure 2.4 presents the block diagram of the moving target indicator radar. In the MTI, Coherent Oscillator (COHO) signal and Stable Local Oscillator (STALO) signal are mixed together and fed to a power amplifier stage, where the pulse modulator controls the power amplifier by switching on and off. Then, the received reflected or echo signal is mixed with the stable local oscillator signal to generate IF signal. IF signal is amplified by an IF amplifier and goes to the phase detector, where by comparing the phase of the IF amplified signal with the phase of the signal coming from the coherent oscillator, the phase difference

is generated to measure the velocity of the target [1], [6], [25].

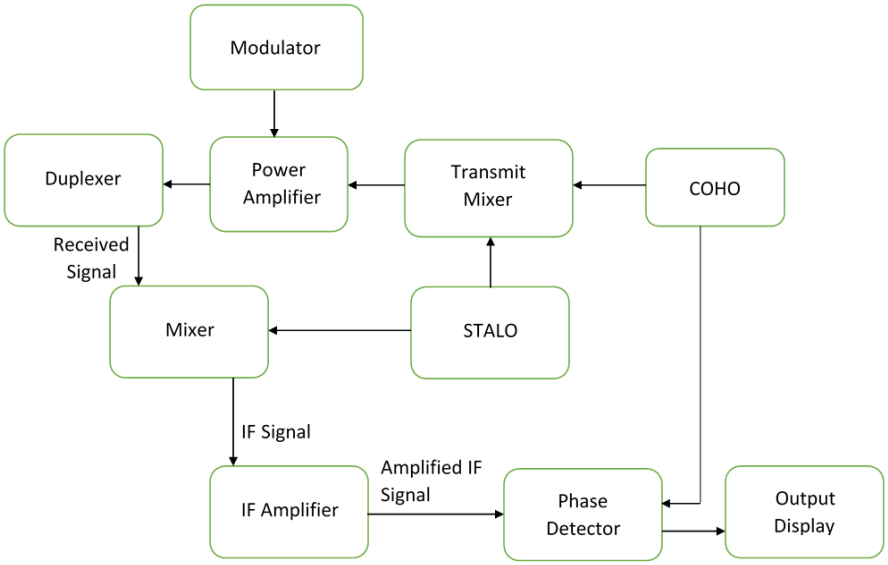

Figure 2.4: Block Diagram of MTI Radar.

2.2 Power Combiners

RF power combiners and splitters have the same circuit, where any RF power combiner can be used as RF power splitter by filliping its circuit. RF power combiners are used to combine several RF signals into one signal while keeping the same characteristic impedance of the signals. Further, Figure 2.5 presents block diagram of RF power combiner, where the two power sources (P1 & P2) are combined together to obtain a high power signal (P3) [29].

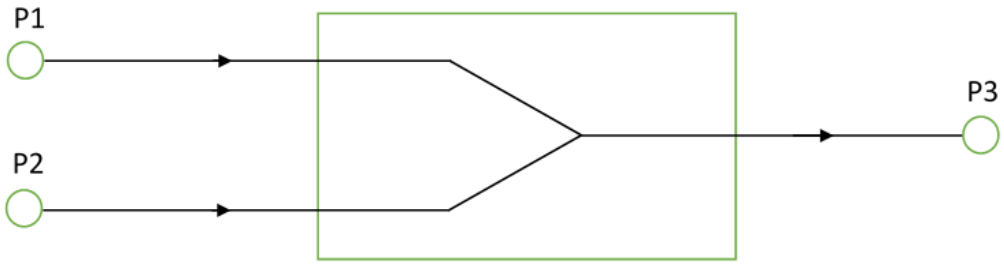

Figure 2.5: RF power combiner.

There are two main types of RF power combiners, namely: Resistive Power Combiner (RPC) and Hybrid Power Combiner (HPC). Resistive power combiners use resistors which produce additional loss to maintain the characteristic impedance of the system. RPCs are known to offer many advantages such as: simplicity since they consist of resistors, wide frequency response, and low fabrication cost [29]. On the other hand, HPCs achieve better performance than RPCs as they reduce the loss level by using transformers. However, HPCs are more complex to implement, have limited frequency range, and incur high fabrication cost [30]. Another power combiner which is widely used in microwave applications is Wilkinson Combiner (WC). This type of combiners uses quarter wave transformers to provide low level of loss, high performance, and low cost. WC is easy to implement on printed circuit boards as quarter wave lines but it has a limited frequency range. The bandwidth of many power combining schemes is very narrow. The common solution is to use a wide-band wilkinson power combiner, which provides a large bandwidth for Ultra-Wide-Band (UWB) applications [31], [32].

There are many methods of power combining such as: Circuit-level, Spatial, and Radial power combining [16], [33]. In circuit-level combining method, the power is divided from an input to many amplifiers connected in parallel by using transmission lines. Depending on the application, these transmission lines can be a Microstrip, Coplanar Waveguide (CPW), Rectangular Waveguide (RW), or a Strip Line. For example, in Monolithic Microwave Integrated Circuits (MMICs), Microstrip and CPW transmission lines are used since they can be integrated easily into such semiconductor processes. Notwithstanding, the power loss in Millimeter Wave (MM wave) frequencies is high compared to other guiding structures like the rectangular waveguide structure [16]. Circuit-level techniques are suitable for monolithic and hybrid amplifier designs. Many possible types of circuit-level power combiners are presented in [34], [35]. However, the 3 dB directional couplers or power dividers are the techniques that most microwave and millimeter wave depend on.

Figure 2.6 shows the concept of the circuit-level combiner. It consists of three stages of splitting, where the signal is split into two output ports which represents the first stage. In the second stage, these two output ports are divided into four ports, where in the third stage, these four ports are then split into 8 ports and each one of them is fed to an amplifier. While for the combining part, the same structure is duplicated and inverted to combine the outputs of the eight amplifiers to produce the desired output. Note that each dividing network can

be implemented by a Wilkinson power divider, lange coupler, and hybrid network [16].

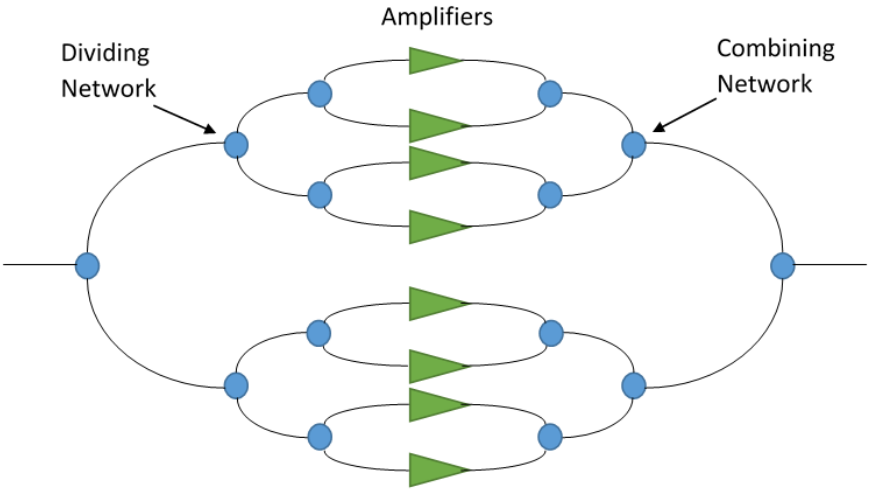

Figure 2.6: Binary Circuit-level Power Combiner.

One of the most appropriate couplers or dividers used in a circuit-level power divider is the 3-port Wilkinson power divider [36]. It divides the input signal into two paths, where the separation between the input signal and output ports is a $\lambda/4$ transmission line.

The spatial power combiner radiates the signal from the source and receives it by an array of amplifying unit cells located in parallel [37]. Specifically, each amplifier amplifies the signal and re-sends the amplified signal into free space. Because of that, the size of the system is large which makes it hard to implement. The approximation of the amplifiers and radiating components results in a high complexity design. The dissipation of heat is mainly more arduous. The spatial power combiner does not use transmission lines to divide the input signal to the amplifiers. Therefore, it does not take into consideration the issue of the total loss in the transmission lines when additional amplifiers are added [16]. Figure 2.7 illustrates the concept of the spatial power combiner. It contains an array of amplifiers located in parallel. They receive, amplify, and radiate the amplified signal into free space. Fundamentally, a very high power combining efficiency can be accomplished in spatial power combiner. The most important issue and concern is the efficiency of the radiating units and the difficulty of uniformly power collecting [16].

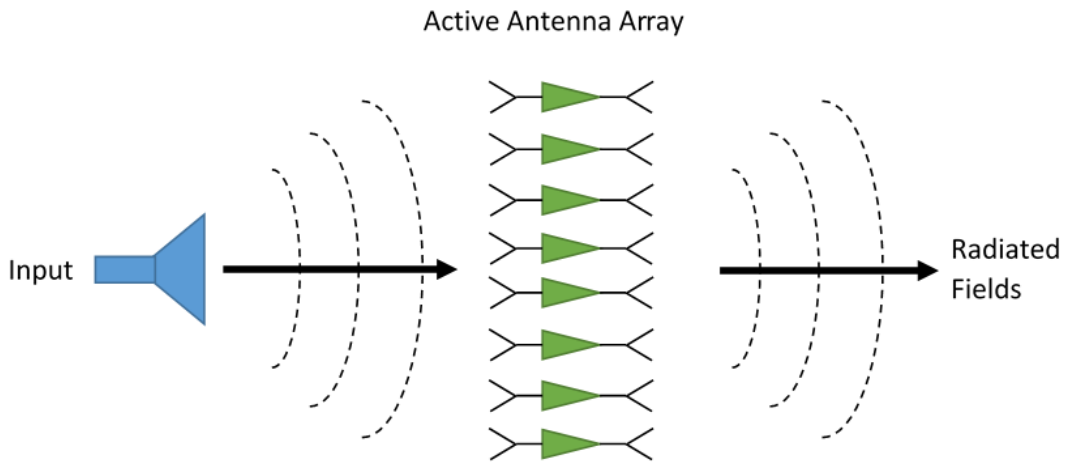

Figure 2.7: Spatial Power Combiner.

Spatial power combining amplifiers are classified based on their array geometry and feeding mechanism. The most two common methods of feeding spatial power combiners are shown in Figure 2.8, where Figure 2.8 (a) shows a spatial power amplifiers that are fed from an input horn far away from the array of amplifiers. Moreover, a multilayer system of lenses is used to direct the energy radiated from the transmit horn to the amplifiers and from the amplifiers to the receive antenna. While Figure 2.8 (b) illustrates that the need of lenses is eliminated as the array of amplifiers is in the feeding field of the horn antennas [16]. Based on the design in Fig. 2.8, there are several advantages in the far-field and near-field methods. In the far-field method, the interaction between the radiating elements of the array and the feeding antenna is minimized, and the feeding beam can be focused, polarized, or reflected by the lenses [38]. Nonetheless, because of the distance between the components of the system, the size of the system is large in microwave and millimeter-wave frequencies. Although, an error in beam focusing may lead to an increase in the overall loss. But, this is not an issue with components having a compact size and short wavelength like in submillimeter-wave frequencies. In the near-field, the size and the weight of spatial power combiner are reduced. Also, due to the direct contact between the horn antennas and the array of amplifiers, the power loss is minimized [16].

The Radial Power Combiner is the most efficient power combiner for summing a large number of power amplifiers. Yet, it is limited to use in real-life due to the design complexity (see Figure 2.9) [39]. Some structures are less complex than radial structure such as: Tree structures. But, they increase the total loss and significantly reduce the overall

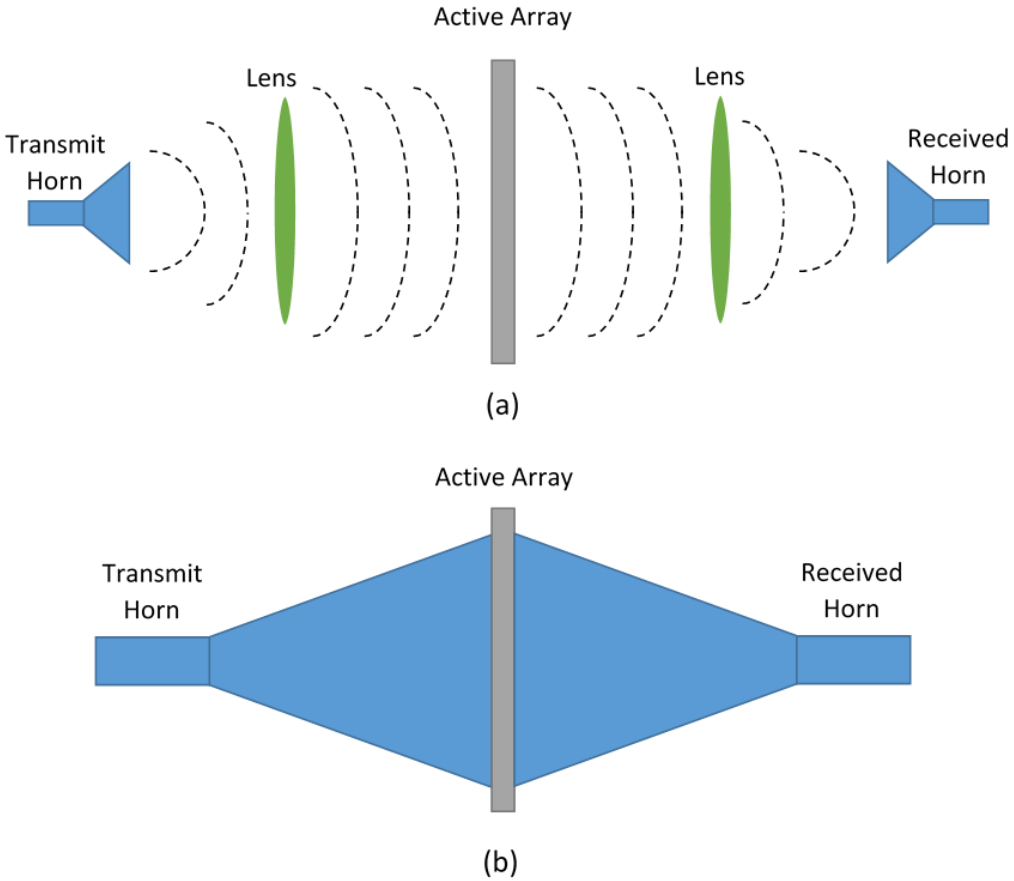

Figure 2.8: Feeding Spatial Power Combiners Techniques (a) the transmitted horn in far-field of amplifying array (b) the transmitted horn in near-field of horn antenna.

efficiency by using several transmission lines. On the other hand, radial power combiner provides an insertion loss less than 0.5 dB and a power combining efficiency grater than 90% over a wide band. The structure of radial combiner allows placing a large number of ports very close to the main feed port, hence the overall loss and the combining path are minimized. Similarly, in order to achieve a low insertion loss and high isolation over the bandwidth, an optimization process of the physical structure has to be applied carefully [40].

2.3 Energy Detection

Energy detection technique is used over a time duration or a bandwidth to detect the signal and distinguish whether the signal is present or absent. It consists of a pre-filter stage, law

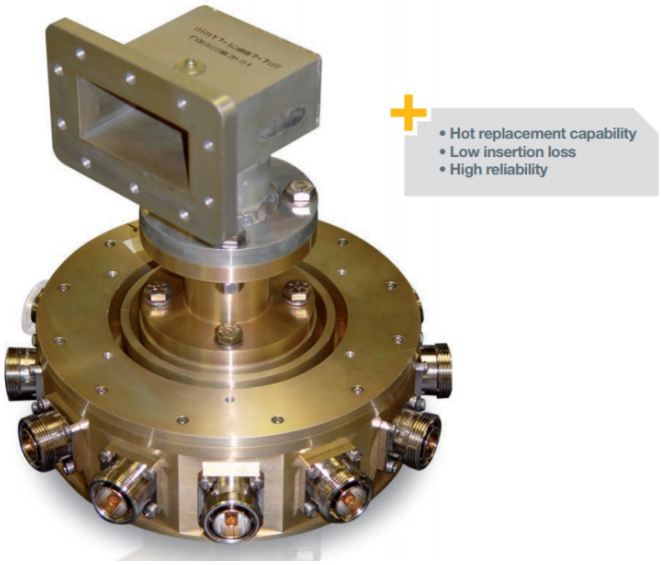

Figure 2.9: Radial Power Combiner [39].

square device, integrator, threshold, and a decision making. Briefly, the signal is fed to a pre-filter stage to reduce the noise power. The energy of the signal is computed and the decision statistic (test statistic) is used to decide on the signal hypothesis by comparing the decision statistic with a threshold. A specific bandwidth is said to be occupied or available if a signal is detected or if only noise level signals are detected [41]-[46], respectively.

The performance of the energy detection technique is illustrated by plotting receiver operating characteristic (ROC) curves or complementary receiver operating characteristic curves. ROC curves are generated by plotting the probability of false alarm P_{fa} versus the probability of detection P_d, where complementary receiver operating characteristic curves are generated by plotting the probability of false alarm versus the probability of missed detection P_m, where $P_m = 1 - P_d$. However, energy detection technique cannot perform efficiently at low signal-to-noise ratio (SNR) [47]-[54].

Chapter 3

Digitally Controlled Microwave Power Combining Systems

3.1 Introduction

It is well known that radar systems need high-power to cover a larger distance, but it can not obtain such high-power from one source. Hence, power combiners are used to combine multiple power sources to produce the required high-power. However, these power sources must be synchronized in time and in-phase to be combined successfully. Theoretically, there are three main properties of any microwave component, which control its functionality: the losslesssness, internal matching, and the reciprocity [55]. However, it has been proven that it is impossible to satisfy all three conditions for three-port networks with the use of only passive elements [20]. An example of such networks is "isolated power combining subsystems" which is used extensively in radar systems. They satisfy two conditions, namely: the losslesssness, and internal matching. But, it comes at the violation of the reciprocity. A possible compensation for such violation can be achieved with an external controller circuit. Figure 3.1 illustrates the normal operation of the traditional power combining network. Each branch consists of an adapter, load and isolator to provide protection circuit, and a power combiner to combine the multiple power sources. When the power sources are in phase and synchronized, the two power sources are combined into a single power source with the same characteristic impedance to produce the required high-power. While in the case of failure, one of the power sources is not synchronized in time or out of phase, 50% of the power will be lost. While the other power source will be reflected and

dissipated in the protection circuit as shown in Figure 3.2. Our proposed system provides a solution to improve the efficiency of the system in the case of failure.

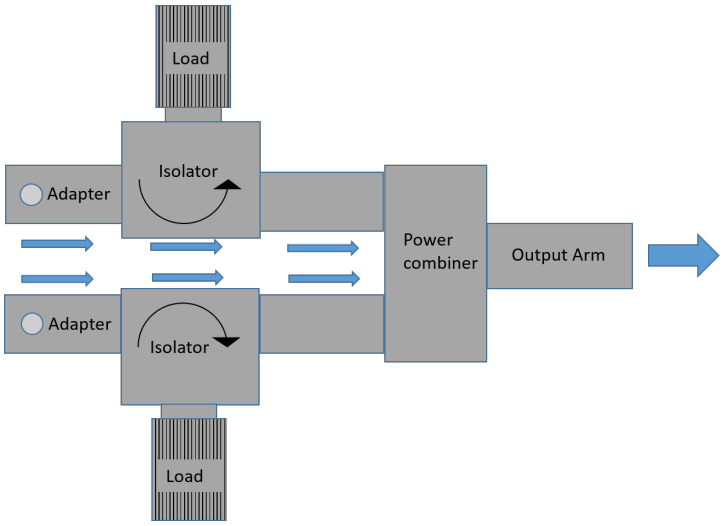

Figure 3.1: Traditional isolated power combining network in the normal operation.

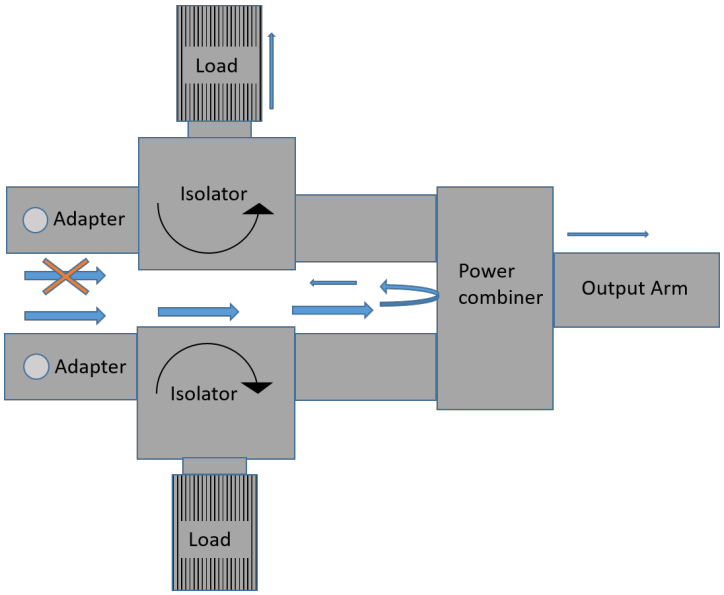

Figure 3.2: Traditional isolated power combining network in the case of failure.

3.2 Proposed System

The proposed system is an innovative solution to minimize the losses of the system by introducing a controlling circuit that samples each branch and direct the signal path to preserve the operation of the system. The proposed subsystem contains multiple components to perform the required functionality. It contains a loop coupler, a controlling circuit, and electrically controlled switches. Specifically, in the normal operation, each coupler takes a power sample of the power source, the controlling circuit controls the switches and directs the output of the power sources to a combiner to achieve high-power as presented in Figure 3.3. Therefore, the proposed system works in the same way as the traditional power combining network in the normal operation. On the other hand, in the case of failure, the controlling circuit senses and defines the power source which is working correctly. Then, it directs the path of the working source to the output by using the electrically controlled switches. Thus, the power of the working source will be saved as shown in Figure 3.4. Variable phase shifters can be used in the system to improve the performance of the system. However, we did not use them in the system.

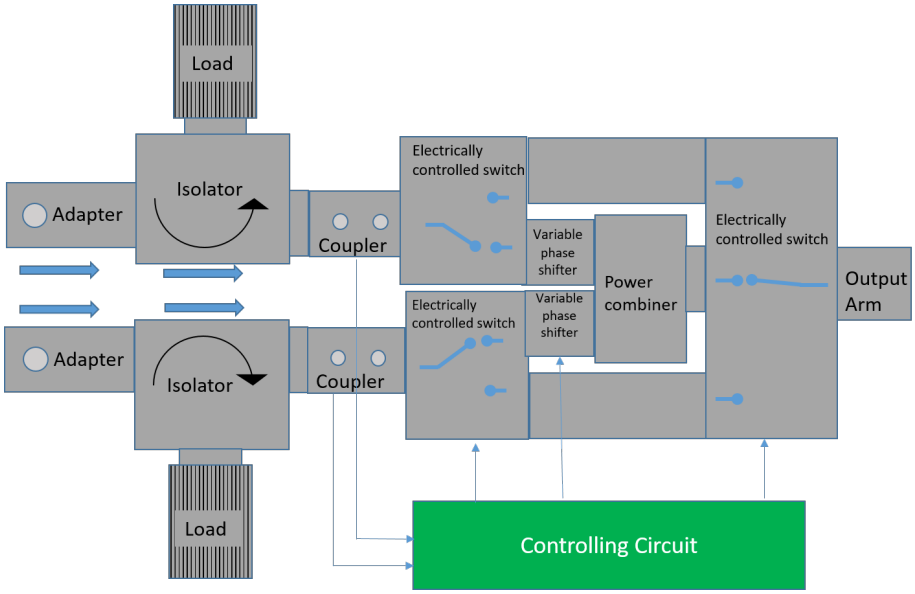

Figure 3.3: Proposed system in the normal operation.

Each branch consists of an adapter, protection circuit, and a loop coupler. The adapter is designed to operate at the required power level, which is limited only by the standard coaxial connector utilized in the system. Also, the isolator and load are needed to provide the protection for the system. The samples coming from the coupler are then digitized, and

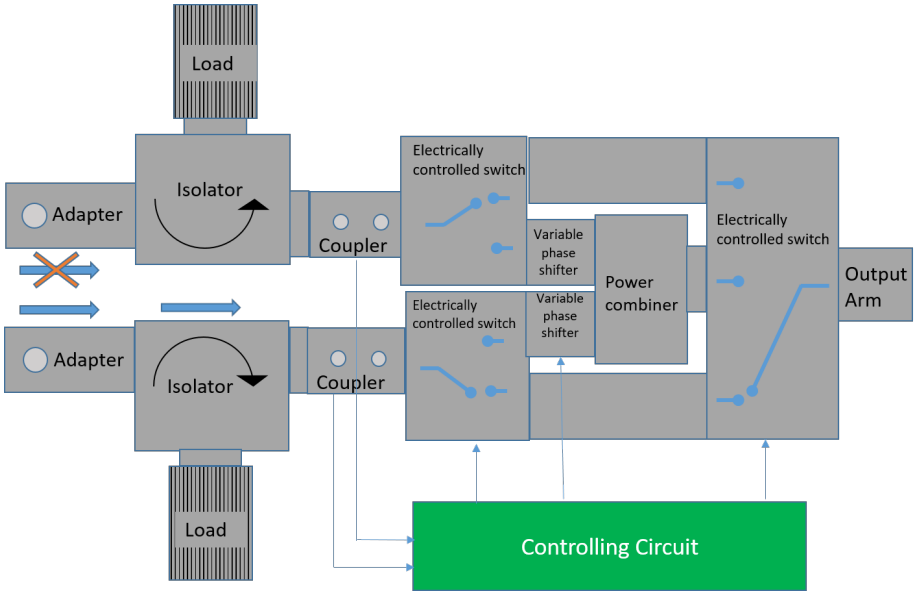

Figure 3.4: Proposed system in the case of failure.

passed to a Digital Signal Processor (DSP) on a Printed Circuit Board (PCB) to analyze, and take the suitable decision. Figure 3.5 illustrates the block diagram of the overall system model for controlling microwave components digitally for high-power radar systems.

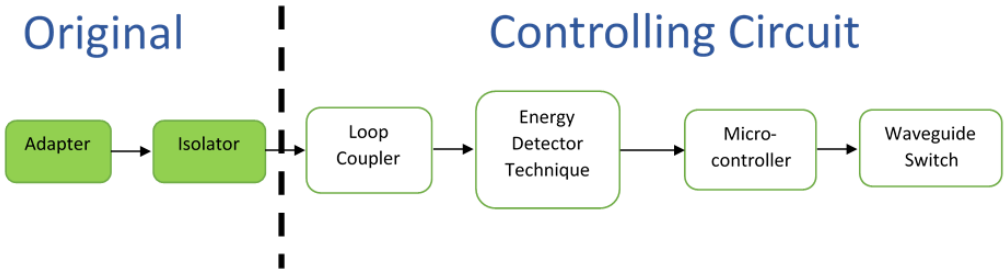

Figure 3.5: Block Diagram of the Overall System.

The sampled RF signal coming from the coupler is fed to a very compact band-pass filter which reduces and rejects the noise power and the undesired signals, respectively. Then, the filtered RF signal is fed to a RMS and Envelope Threshold Detection board (ADL 5904) which produces digital control output and it detects if there is an RF signal or not. If ADL 5904 detects the RF signal (hypothesis H_1), it produces a digital control output (Logic High) which means that the signal is present. The digital control output is passed to the Micro-controller (ATmega328). The micro-controller uses dual full bridge driver (L298) to set the suitable direction of the waveguide switch (WR229) depending on the digital

control output coming from the ADL 5904. On the other hand, if the ADL 5904 does not detect the RF signal (hypothesis H_0). It will produce a digital control output (logic low), which will be passed to the micro-controller stage. The micro-controller is programmed to choose the appropriate direction of the waveguide switch by using the dual full bridge driver. Figure 3.6 illustrates the block diagram of the energy detection technique. It consists of a pre-filter, a square law device, an integrator, threshold, and Decision making.

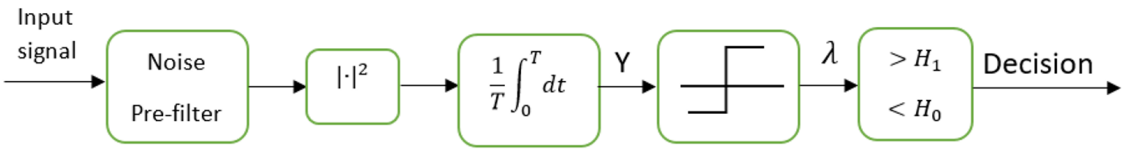

Figure 3.6: Block Diagram of Energy Detection Technique.

The signal is fed to a pre-filter stage to reduce the noise power and reject the unwanted signals. Usually, it is a band-pass filter. The energy of the filtered signal is obtained. Therefore, the presence and the absence of the signal can be determined by comparing the test statistic with a threshold. More precisely, if the test statistic exceeds the threshold, so the decision is hypothesis H_1 indicating that the signal is present and the channel is occupied. On the other hand, when the test statistic is less than the threshold, the decision is hypothesis H_0 which corresponds to the absence of the signal. In the next chapter, we will present the pre-filtering stage and illustrate the traditional band-pass filter and the proposed band-pass filter where we used coupled structure technique to have a very compact size.

3.3 Summary

In this chapter, we discussed the limitations of the traditional power combining network in the normal operation and in the case of failure, which occurred when one of the power sources is not synchronized or out of phase, resulting in reflection for the working power source and dissipated in the circuit protection. We showed how the proposed system improves the efficiency in the case of failure. It directs the path of the working power source into the output to save the power of the working source. We proposed adding two loop couplers to take samples of the power sources. These samples will be passed to the controlling circuit. The controlling circuit senses the working power source and direct it into the output via the electrically controlled switches.

Chapter 4

Ultra-Wideband Printed Bandpass Filter Based on Coupled-Line Resonator Loading

4.1 2-port Network

In this chapter, we are going to focus on designing a band-pass filter with a frequency range from 2 GHz to 7 GHz, which is essential to reduce the noise level. Firstly, we will present a quick description of the scattering parameters of 2-port network. Figure 4.1 illustrates the scattering parameters for 2-port network.

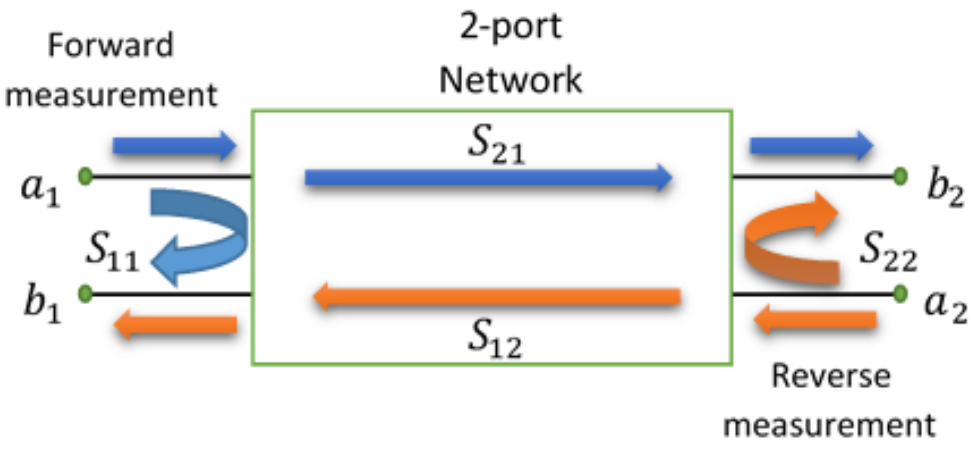

Figure 4.1: Scattering parameters for 2-port network.

As shown in Fig, 4.1. S_{11}, S_{12}, S_{21}, and S_{22} represent the scattering parameters, a_1 and a_2 are the incident waves, b_1 and b_2 are the outgoing waves [56]. They are given as:

$$\begin{bmatrix} b_1 \\ b_2 \end{bmatrix} = \begin{bmatrix} S_{11} & S_{12} \\ S_{21} & S_{22} \end{bmatrix} * \begin{bmatrix} a_1 \\ a_2 \end{bmatrix}, \tag{4.1}$$

S_{11} is the input reflection coefficient, referred as the ratio of the outgoing wave b_1 over the incident wave a_1. S_{21} is the forward transmission coefficient, defined as the ratio of the outgoing wave b_2 over the incident wave a_1. S_{12} is the reverse transmission coefficient, known as the ratio of the outgoing wave b_1 over the incident wave a_2. S_{22} is the output reflection coefficient, referred as the ratio of the outgoing wave b_2 over the incident wave a_2 [56]. In the following section, we present several types of filters and the transformation from a low pass filter to a high pass filter or a band-pass filter.

4.2 Types of Filters

Filters are used to pass the desired signals over a specific bandwidth, to remove the unwanted signals, and to reduce the noise level. There are many types of filters such as: Low Pass Filter (LPF), High Pass Filter (HPF), and Band-pass Filter (BPF).
Figure 4.2 illustrates the frequency response of an ideal LPF, HPF, and BPF, respectively, where f_c represents the cut-off frequency, f_{min} is the the minimum frequency, f_{max} is the maximum frequency, and f_0 is the central frequency. However, it is well known that an ideal filter is not feasible.

A traditional methodology for the implementation of different types of filters is to start with the implementation of the LPF prototype. This process is followed by a transformation from LPF to HPF or BPF according to the transformation illustrated in Figure 4.3. More precisely, LPF can be transformed to a HPF by replacing each series inductor (L) by a series capacitor (C), and each shunt capacitor by a shunt inductor. On the other hand, a LPF can be transformed to a BPF by converting each of its series inductor to a series of inductor and capacitor, and each shunt capacitor is transformed to a shunt of capacitor and inductor [57]. In sections 4.3, we highlight two classical polynomials deployed in forming specific filters responses.

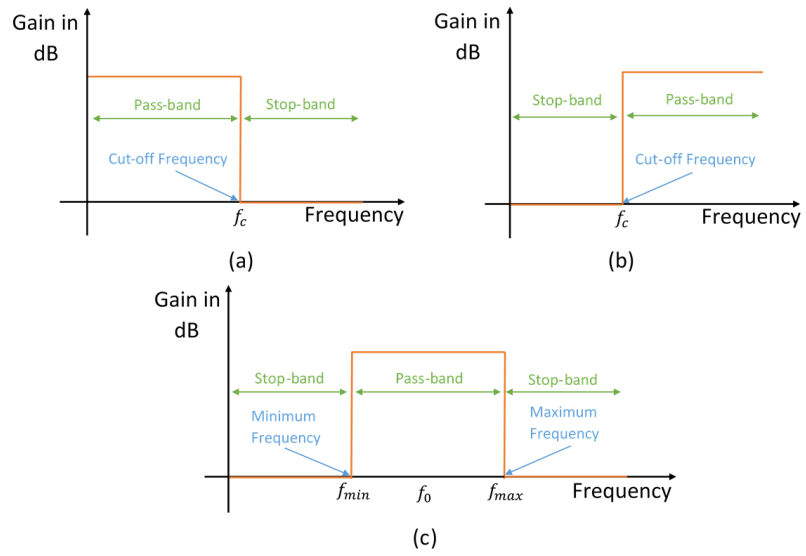

Figure 4.2: Frequency Response of Some Types of Filters (a) Frequency Response of a LPF (b) Frequency Response of a HPF (c) Frequency Response of a BPF.

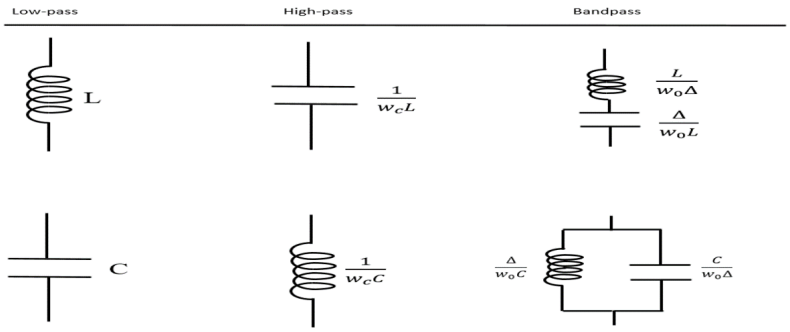

Figure 4.3: Transformation from LPF to HPF or BPF.

4.3 Filter Response

There are many types of filter responses such as: equal ripple (Chebyshev), maximally flat, and elliptic response. Equal ripple response referred as Chebyshev. In this section, we are going to focus only on both the maximally flat and the Chebyshev responses. For the Chebyshev response, it has ripples within the pass-band with a sharper stop-band response than maximally flat response as indicated in Figure 4.4. Tables 4.1 & 4.2 show the normalized equal ripple $(-0.5\ dB\ \&\ -3\ dB)$ LPF for different order (N) and the corresponding inductors and capacitors for each order [57]. These tables are used to form a normalized LPF prototype.

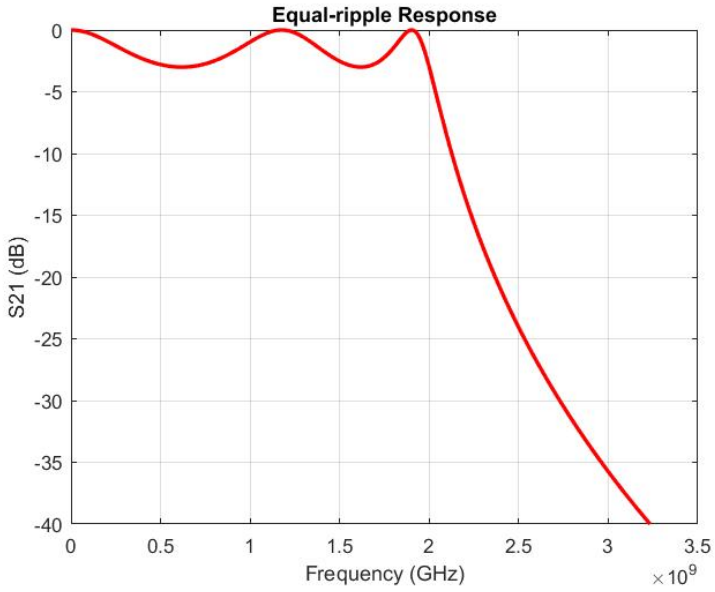

Figure 4.4: Equal-ripple response.

Table 4.1: Element Values for Equal Ripple $(-0.5\ dB)$ Low-pass Filter Prototypes.

N	g_1	g_2	g_3	g_4	g_5	g_6	g_7	g_8	g_9	g_{10}	g_{11}
1	0.6986	1.0000									
2	1.4029	0.7071	1.9841								
3	1.5963	1.0967	1.5963	1.0000							
4	1.6703	1.1926	2.3661	0.8419	1.9841						
5	1.7058	1.2296	2.5408	1.2296	1.7058	1.0000					
6	1.7254	1.2479	2.6064	1.3137	2.4758	0.8696	1.9841				
7	1.7372	1.2583	2.6381	1.3444	2.6381	1.2583	1.7372	1.0000			
8	1.7451	1.2647	2.6564	1.3590	2.6964	1.3389	2.5093	0.8796	1.9841		
9	1.7504	1.2690	2.6678	1.3673	2.7239	1.3673	2.6678	1.2690	1.7504	1.0000	
10	1.7543	1.2721	2.6754	1.3725	2.7392	1.3806	2.7231	1.3485	2.5239	0.8842	1.9841

On the other hand, maximally flat response is also known as Butterworth response. It provides the flattest frequency response and does not have ripples in the pass-band as shown in Figure 4.5. In the following section, one of these filter polynomials will be deployed to design LPF based on the stepped impedance filter technique. Table 4.3 gives the element values for maximally flat LPF [57].

Table 4.2: Element Values for Equal Ripple $(-3\ dB)$ Low-pass Filter Prototypes.

N	g_1	g_2	g_3	g_4	g_5	g_6	g_7	g_8	g_9	g_{10}	g_{11}
1	1.9953	1.0000									
2	3.1013	0.5339	5.8095								
3	3.3487	0.7117	3.3487	1.0000							
4	3.4289	0.7483	4.3471	0.5920	5.8095						
5	3.4817	0.7618	4.5381	0.7618	3.4817	1.0000					
6	3.5045	0.7685	4.6061	0.7929	4.4641	0.6033	5.8095				
7	3.5182	0.7723	4.6386	0.8039	4.6386	0.7723	3.5182	1.0000			
8	3.5277	0.7745	4.6575	0.8089	4.6990	0.8018	4.4990	0.6073	5.8095		
9	3.5340	0.7760	4.6692	0.8118	4.7272	0.8118	4.6692	0.7760	3.5340	1.0000	
10	3.5384	0.7771	4.6768	0.8136	4.7425	0.8164	4.7260	0.8051	4.5142	0.6091	5.8095

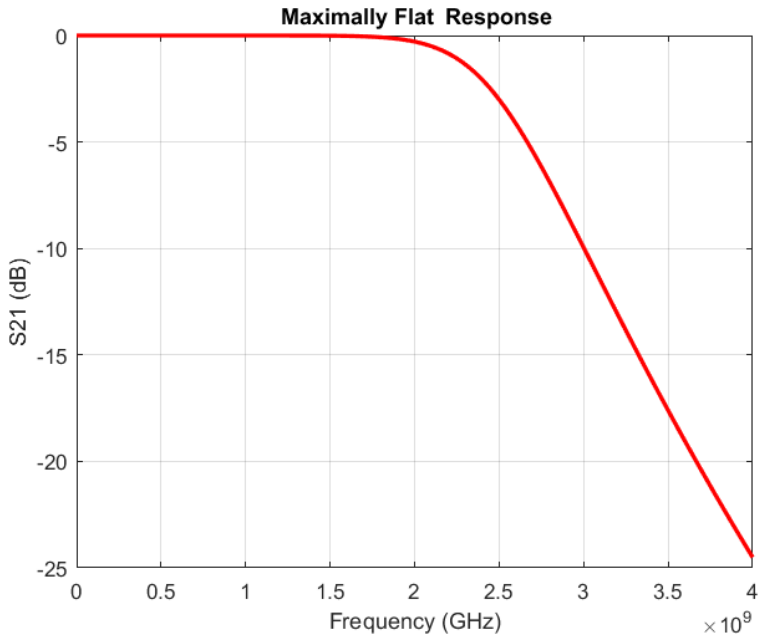

Figure 4.5: Maximally flat response.

4.4 Traditional Filters

In this section, we will explain the general design procedure based on a specific type of filter implementation as an example. The selected type of filters is the stepped impedance filter, which can be deployed to design low pass filters only [57]. This type of filters cascades high impedance and low impedance transmission lines to realize capacitors and inductors, respectively. This type of filters is selected as it has a relatively compact size, where each section of the filter has to be smaller than quarter wavelength. This gives an indication about the expected overall size of traditional filters in the required frequency band. Figure 4.6 shows the traditional design procedure of any filter at the microwave frequencies.

Table 4.3: Element Values for Maximally Flat Low-pass Filter Prototypes.

N	g_1	g_2	g_3	g_4	g_5	g_6	g_7	g_8	g_9	g_{10}	g_{11}
1	2.0000	1.0000									
2	1.4142	1.4142	1.0000								
3	1.0000	2.0000	1.0000	1.0000							
4	0.7654	1.8478	1.8478	0.7654	1.0000						
5	0.6180	1.6180	2.0000	1.6180	0.6180	1.0000					
6	0.5176	1.4142	1.9318	1.9318	1.4142	0.5176	1.0000				
7	0.4450	1.2470	1.8019	2.0000	1.8019	1.2470	0.4450	1.0000			
8	0.3902	1.1111	1.6629	1.9615	1.9615	1.6629	1.1111	0.3902	1.0000		
9	0.3473	1.0000	1.5321	1.8794	2.0000	1.8794	1.5321	1.0000	0.3473	1.0000	
10	0.3129	0.9080	1.4142	1.7820	1.9754	1.9754	1.7820	1.4142	0.9080	0.3129	1.0000

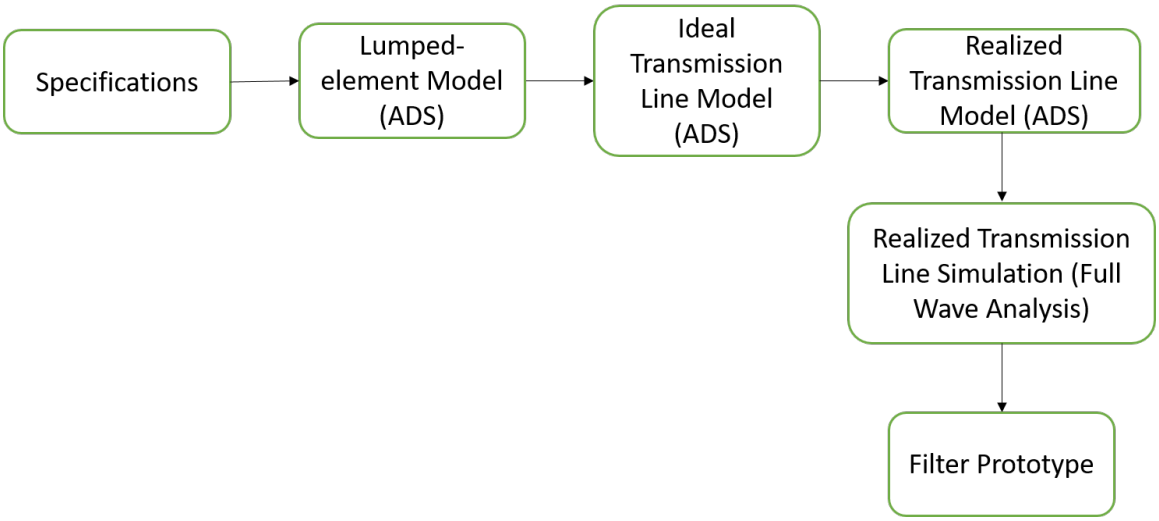

Figure 4.6: Design Procedure of Filters.

The first step in designing any filter is to define the specifications such as: the order of the filter N, the type of the filter, the response of the filter, and the frequency range. The second step is to design the filter in lumped-element form by using capacitors and inductors in any microwave simulation softwares such as: Advanced Design System (ADS), or Toolkit for Interactive Network Analysis (TINA). These capacitors and inductors can be obtained by using the following equations [57]:

$$\begin{aligned} C_k' &= \frac{C_k}{w_c Z_0}, \\ L_k' &= \frac{Z_0 L_k}{w_c}, \end{aligned} \tag{4.2}$$

where C_k and L_k are the normalized element values based on the selected response, w_c is the reference angular frequency ($w_c = 2\pi f_c$). For design validation, the proposed filter can be modeled by any software package such as ADS or TINA. There are two models of

the transmission line, namely: ideal transmission line model, and realized transmission line model. Furthermore, the ideal transmission line model can be implemented by inserting the electrical length (βl_k) of the normalized element values as in ADS, where electrical lengths can be computed using [57]

$$\begin{aligned} \beta l_k &= \frac{C_k Z_l}{Z_0}, \\ \beta l_k &= \frac{Z_0 L_k}{Z_h}, \end{aligned} \tag{4.3}$$

where Z_0 represents the line impedance, Z_l & Z_h are the lowest and highest practical line impedance, respectively. Alternatively, the transmission line model can be implemented by inserting the transmission delay (τ) of the normalized element values. The transmission delay can be expressed as

$$\tau_k = \frac{\theta_k}{2\pi f_c}, \tag{4.4}$$

where θ is the radian value of the electrical length. However, the ideal transmission line model is practically impossible to implement. This led to the use of the practical model which is the realized transmission line model. The latter is designed by calculating the widths and lengths of the inductors and capacitors for a microstrip line technology. Moreover, these widths and lengths can be obtained using LineCalc tool in ADS. The final validation step is performed through full wave analysis for the designed filter, where the selected simulation package is Computer Simulation Technology (CST). However, traditional filters do not have an extreme compact size which is an important matter in microwave engineering.

The order N of the filter is the key parameter to improve the rejection slope of the filter. However, it increases the size of the filter knowing that each section has a length of quarter wavelength. Based on that, when the central frequency of a band-pass filter or the cut-off frequency of a low pass filter or a high pass filter decreases, the filter overall size increases. The primary objective is to implement a band-pass filter with a frequency range from 2 GHz to 7 GHz in order to implement the desired filter. One method is to design a low pass filter to set the maximum frequency (7 GHz), and to design a high pass filter to set the minimum frequency (2 GHz).

Using stepped-impedance to implement a low pass filter will result a relatively compact response. Table 4.4 gives the electrical lengths, widths, and lengths of a stepped-impedance low pass filter. It has a cut-off frequency 7 GHz, $5th$ order, the high and low characteristic

impedance lines are $100\ \Omega$ and $20\ \Omega$, respectively. Figure 4.7 illustrates the ideal transmission line model of the stepped impedance low pass filter.

Table 4.4: Dimensions of the stepped-impedance LPF.

Z_l, Z_h	Electrical length (°)	Width (mm)	Length (mm)
20	14.16	10.72	0.83
100	46.35	0.66	3.19
20	45.84	10.72	2.7
100	46.35	0.66	3.19
20	14.16	10.72	0.83

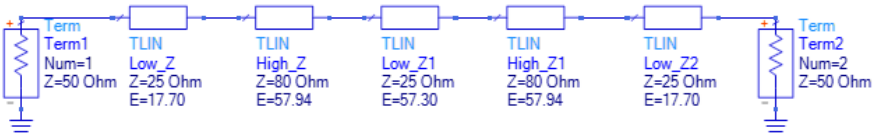

Figure 4.7: Ideal transmission line model of the stepped-impedance LPF.

Figure 4.8 shows the frequency response of the ideal transmission line model of the stepped impedance low pass filter. The realized transmission line model of the stepped-impedance on ADS is illustrated in Figure 4.9. The frequency response of the realized transmission line model is given in Figure 4.10. Furthermore, Figure 4.11 shows a 3D view of the simulated model in CST, while the simulated response is shown in Figure 4.12.

Based on the proposed filter design, the length of the stepped-impedance is 3.1 cm. However, we still need to add a high pass filter with a cut-off frequency of 2 GHz to the stepped-impedance low pass filter to implement the band-pass filter. The high pass filter should be designed with a cut-off frequency of 2 GHz. The length of the traditional band-pass filter with a frequency range from 2 GHz to 7 GHz is around 9 cm. This estimated overall size is calculated based on any 5 order filter with a single stage size of quarter wavelength. The considered wavelength is the center value of the target band, 4.5 GHz. Based on that, we implemented our proposed filter by using another design concept, which will be illustrated in the following section.

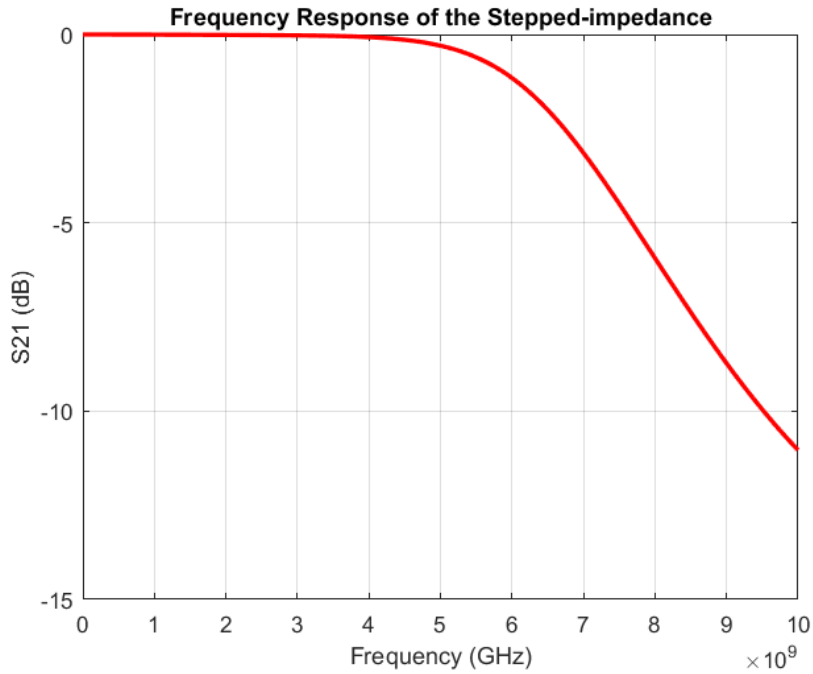

Figure 4.8: Frequency response of the ideal transmission line model of the stepped-impedance LPF.

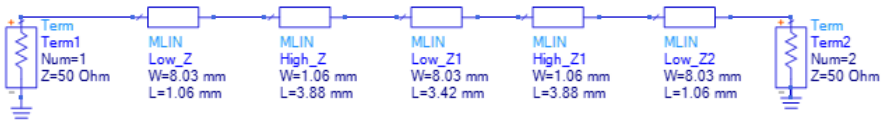

Figure 4.9: Realized transmission line model of the stepped-impedance LPF.

4.5 Proposed Filter

The proposed filter is a novel compact design for Ultra-Wideband (UWB) BPF using a coupled line resonator. It consists of two identical wideband coupling sections as input and output stages. In addition, the middle section is loaded with two identical parallel resonators to enhance the out of band rejection by introducing transmission zeros. Also, a stepped transform is added at the input and output coupling stages to enhance the overall matching. The proposed filter is implemented using microstrip line technology to be fabricated on a Printed Circuit Board (PCB). The proposed design offers an UWB covering the S, C and G bands used for radar applications starting at 2 GHz up to 7 GHz. The proposed filter has a matching level exceeds 19 dB, which means that $\frac{1}{10^{19/10}} = 0.0126$ of the signal passing the proposed filter will be reflected. The overall size of the proposed filter is

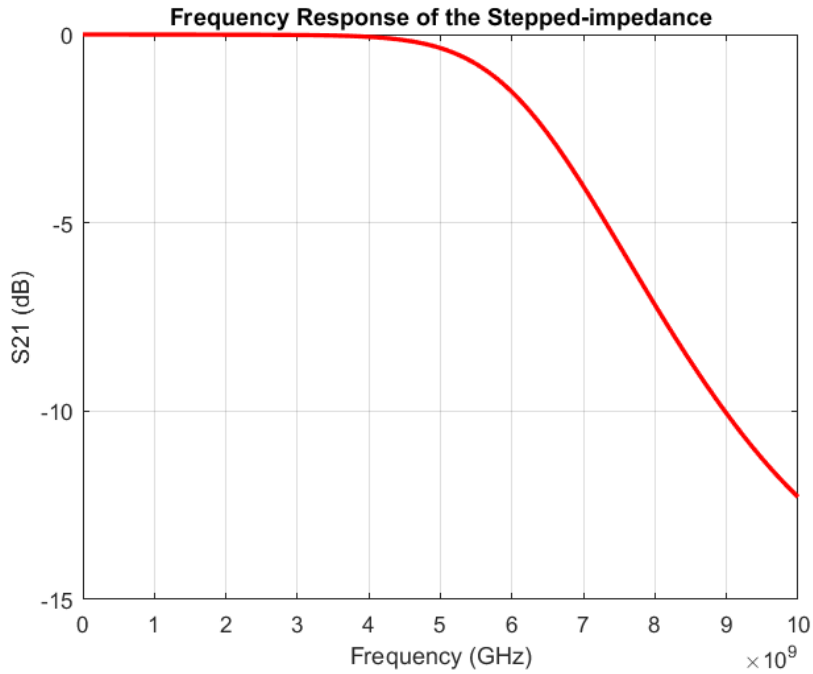

Figure 4.10: Frequency response of the ideal transmission line model of the stepped-impedance LPF.

shorter than a half wavelength at the center frequency. The initial proposed filter structure with stepped transforms is presented in Figure 4.13. The proposed filter is printed on a TMM4 substrate with a dielectric constant of 4.5 and dielectric height of 1.524 mm, and the input line width is chosen to provide 50Ω input impedance. The dimensions of the input and output transitions are listed in Table 4.5.

Table 4.5: Dimensions of the input and output transitions.

Variable	Value (mm)	Variable	Value (mm)
W_1	2.88	L_1	0.75
W_2	2	L_2	0.75
W_3	1.8	L_3	0.75
W_4	0.48	L_4	5.8
W_5	0.4	L_5	0.8
W_6	1.86	L_6	6.4

The gaps between the couplers were chosen to be $g = 0.25$ mm and $g_1 = 0.5$ mm. These dimensions are optimized to achieve deep matching level without paying attention to the out-of-band rejection in this stage of the design, where it will be adjusted in later step. The performance of proposed filter (scattering parameters) is shown in Figure 4.14. The

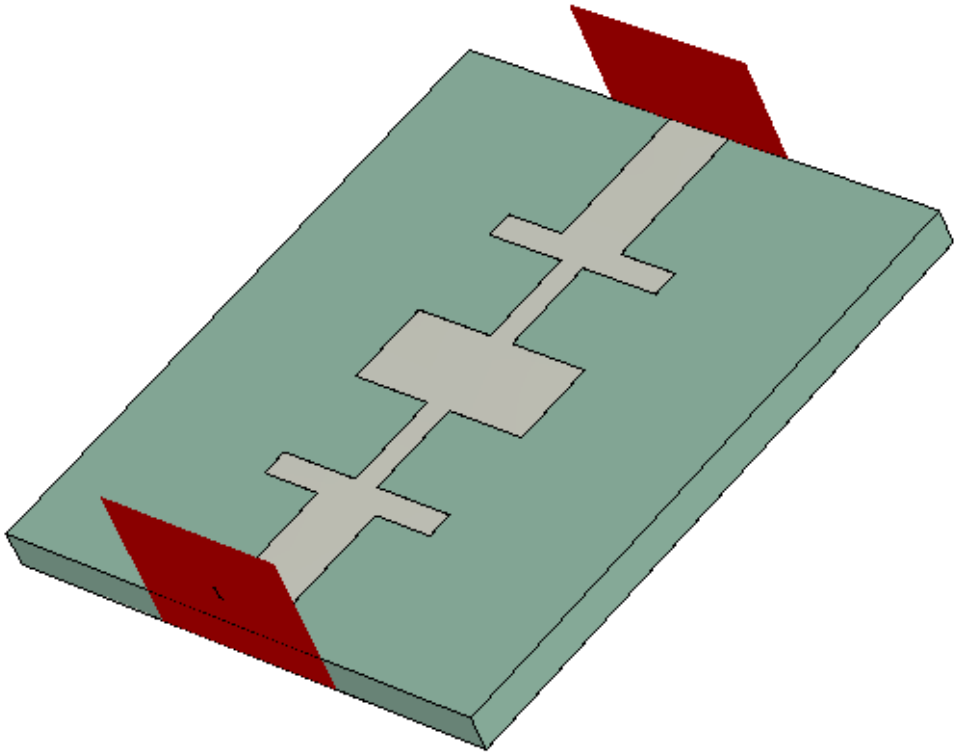

Figure 4.11: Realized transmission line model of the stepped-impedance low pass filter.

pass-band frequency of the filter is between $2.7 - 6$ GHz, where the stepped transformer improved the overall matching with a return loss exceeding 19 dB.

A symmetric coupled-line resonator is added to the filter to enhance the performance of the out-band rejection. The layout of the proposed filter is given in Figure 4.15, and the dimensions used in the design are listed in Table 4.6. The gap between the couplers were chosen as follows: g$= 0.3$mm, $g_1 = 0.25$mm, $g_2 = 0.1524$mm, and $g_3 = 0.11$mm. The enhancement of the out-band rejection is noticeable in Figure 4.16 which represents the frequency response of the proposed filter. Moreover, the rejection is beyond 26 dB at 8.6 GHz. The fabricated proposed band-pass filter is shown in Figure 4.17. Figure 4.18 illustrates the scattering parameters of the fabricated filter with the Sub-Miniature version A (SMA) connectors. The insertion loss (radiated power) is about 2 dB, which means that any signal passes the proposed filter, it will lose around 2 dB of its power directly. It has a matching level below -12 dB and the rejection is approximately below 24 dB at 8.6 GHz [58]. Figure 4.19 illustrates the scattering parameters of the simulated and measured values, where we used the N5227A PNA Microwave Network Analyzer from Agilent (

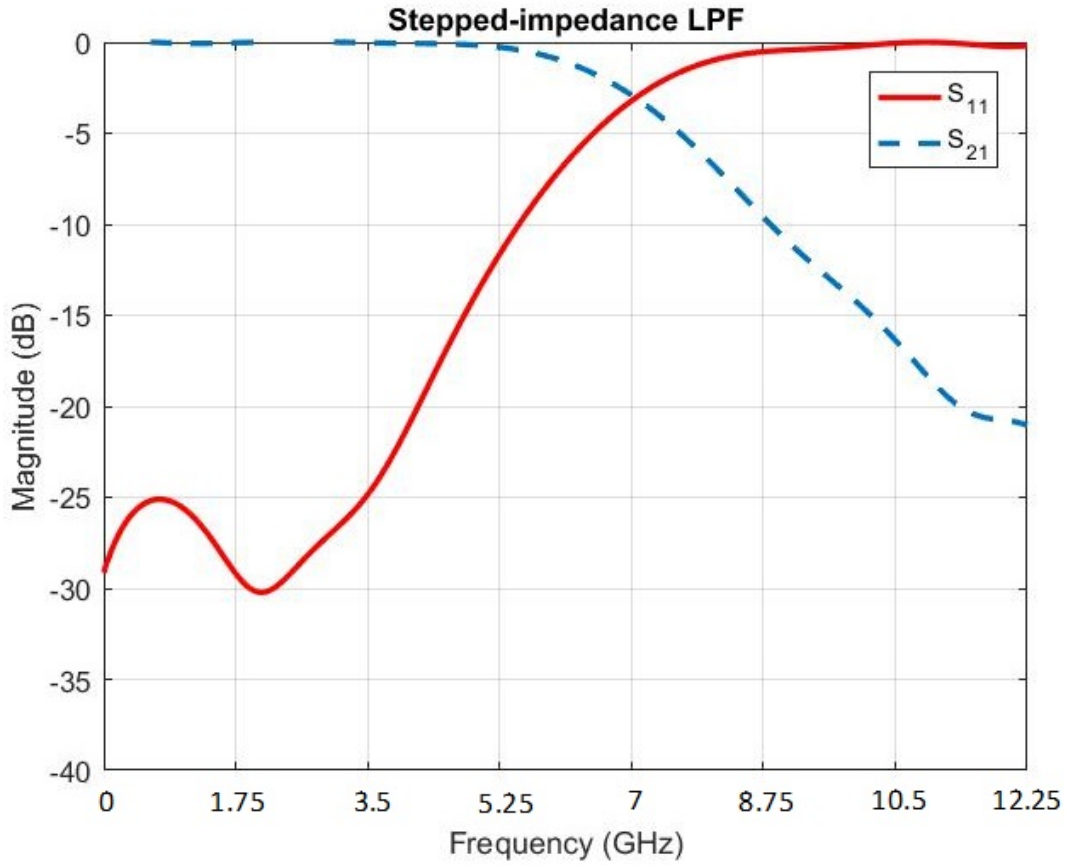

Figure 4.12: Scattering parameters of the realized transmission line model of the stepped-impedance low pass filter.

Keysight Technologies) to measure the filter response. There is around 7 dB difference between the simulated and measured scattering parameters due to the manufacturing tolerances. In addition, the SMA connector is welded to the line manually, which leads to clear imperfections. This soldering point results in extra radiation losses. The significant radiation losses can be reduced through using other implementation technologies such as ridge gap waveguide with wide bandwidth [59]-[63].

4.6 Summary

In this chapter, we deployed the stepped impedance filter, one of the traditional filter implementation technique, to produce a filter in the objective band. This step is performed to evaluate the expected overall size of the required filter. This step resulted in a LPF of

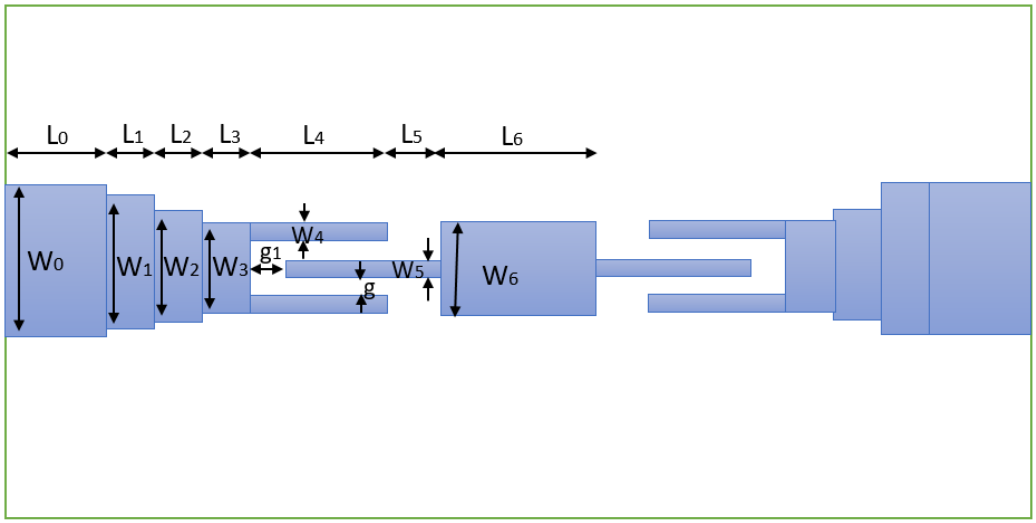

Figure 4.13: Structure top view of the proposed band-pass filter.

Table 4.6: Dimensions of the proposed filter.

Variable	Value (mm)	Variable	Value (mm)
W_1	2.84	L_1	1.05
W_2	1.06	L_2	0.959
W_3	5.02	L_3	0.593
W_4	0.28	L_4	9.318
W_5	0.4	L_5	2.079
W_6	0.65	L_6	3.33
W_7	0.42	L_7	2.16
W_8	0.33	L_8	1.79
W_9	0.48	L_9	2.50

more than 3 cm size, where another high pass filter is required to form the objective band pass filter. Through this detailed assessment, we recognized that the traditional filter design methodologies will produce a relatively large filter design. Hence, we direct our research toward the design of more compact structure keeping the same objective response. We proposed using coupled structure technique to have a very compact band-pass filter. We proposed using a stepped transform to the input and output coupling stages to enhance the overall matching level. Finally, a symmetric coupled-line resonator is added to the proposed filter to improve the performance of the out-band rejection. The fabricated proposed filter has a matching level below 12 dB with an out of band rejection beyond 25 dB at 8.6 GHz.

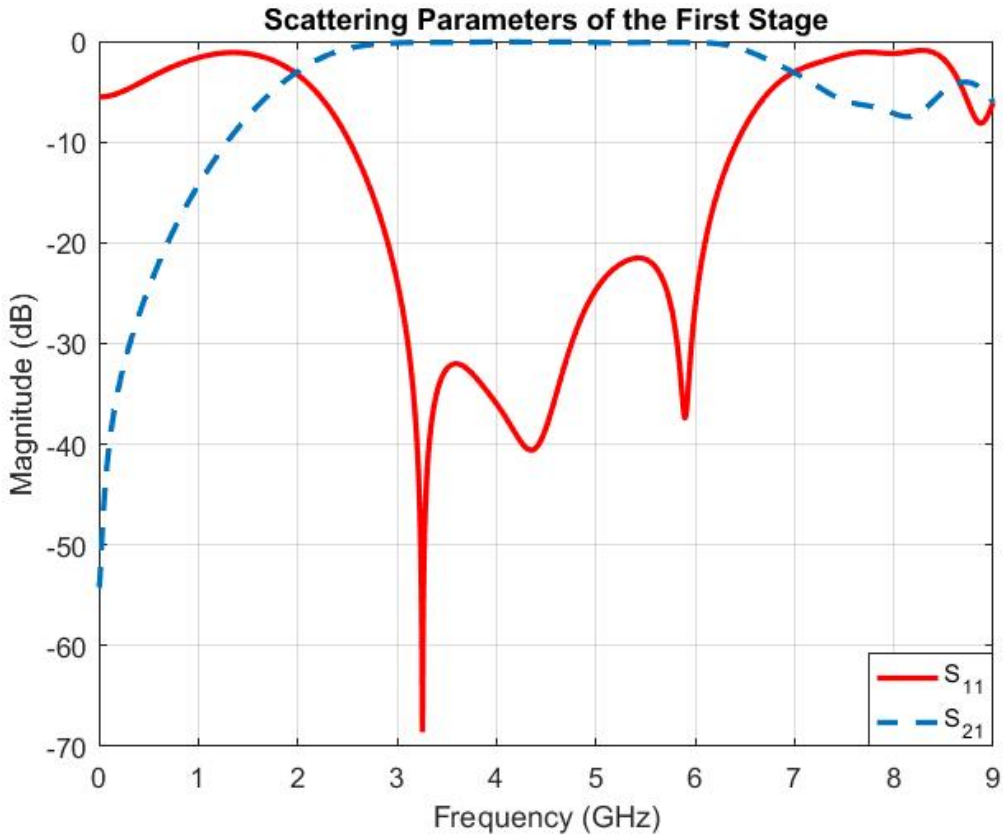

Figure 4.14: Scattering parameters of the first stage of the proposed band-pass filter.

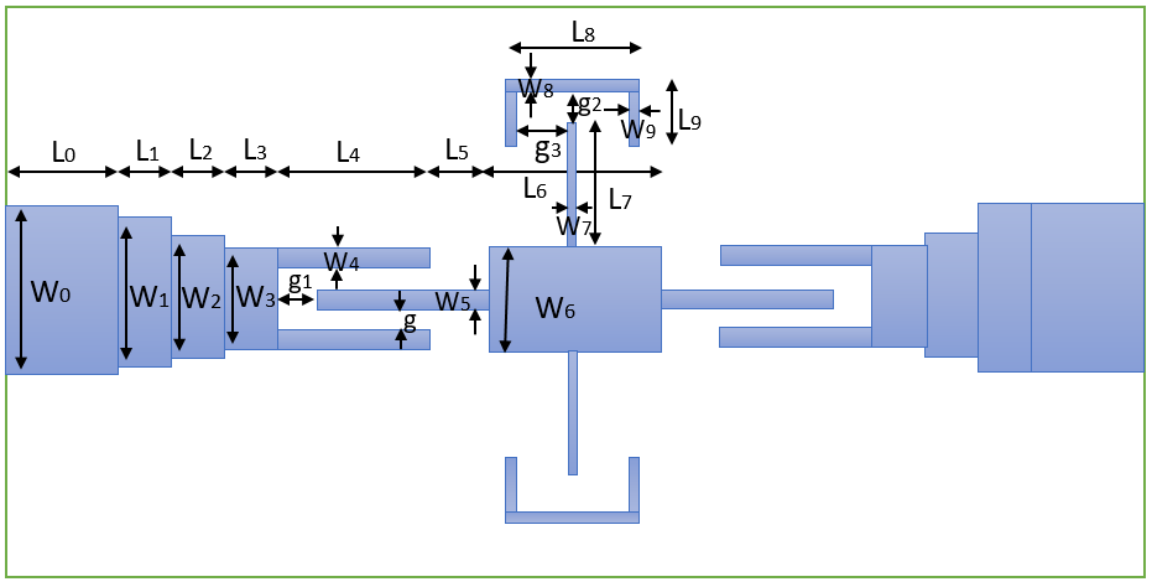

Figure 4.15: Structure top view of the final design of the proposed filter.

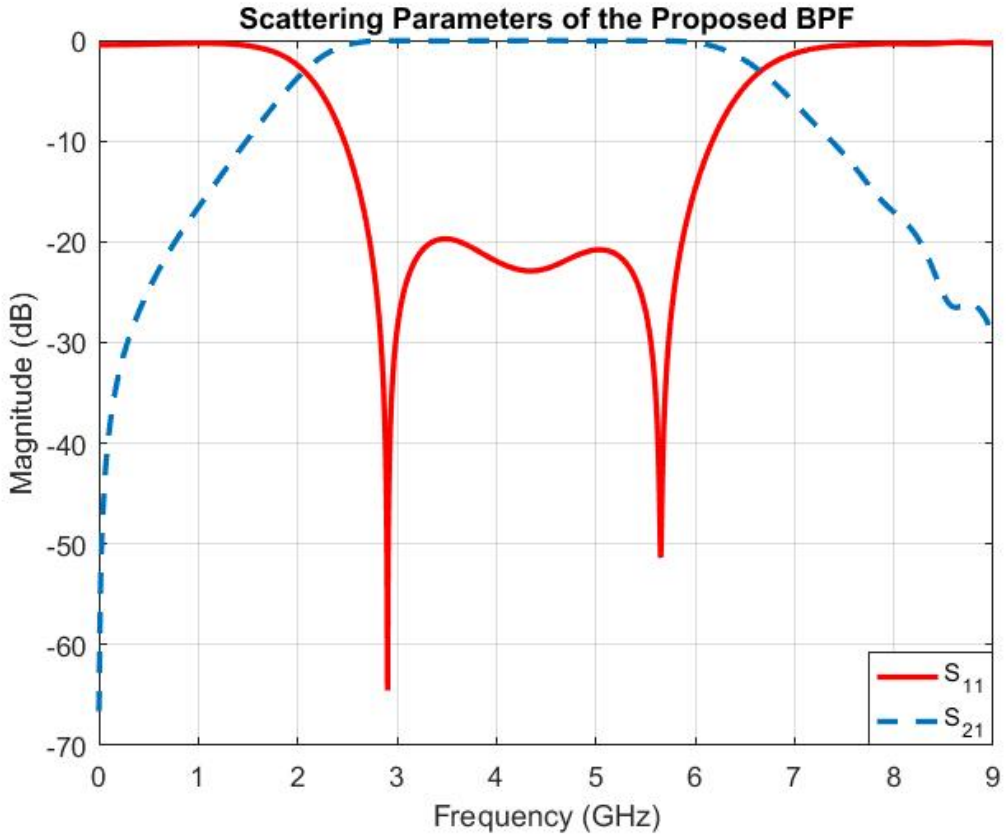

Figure 4.16: Scattering parameters of the final design of the proposed filter.

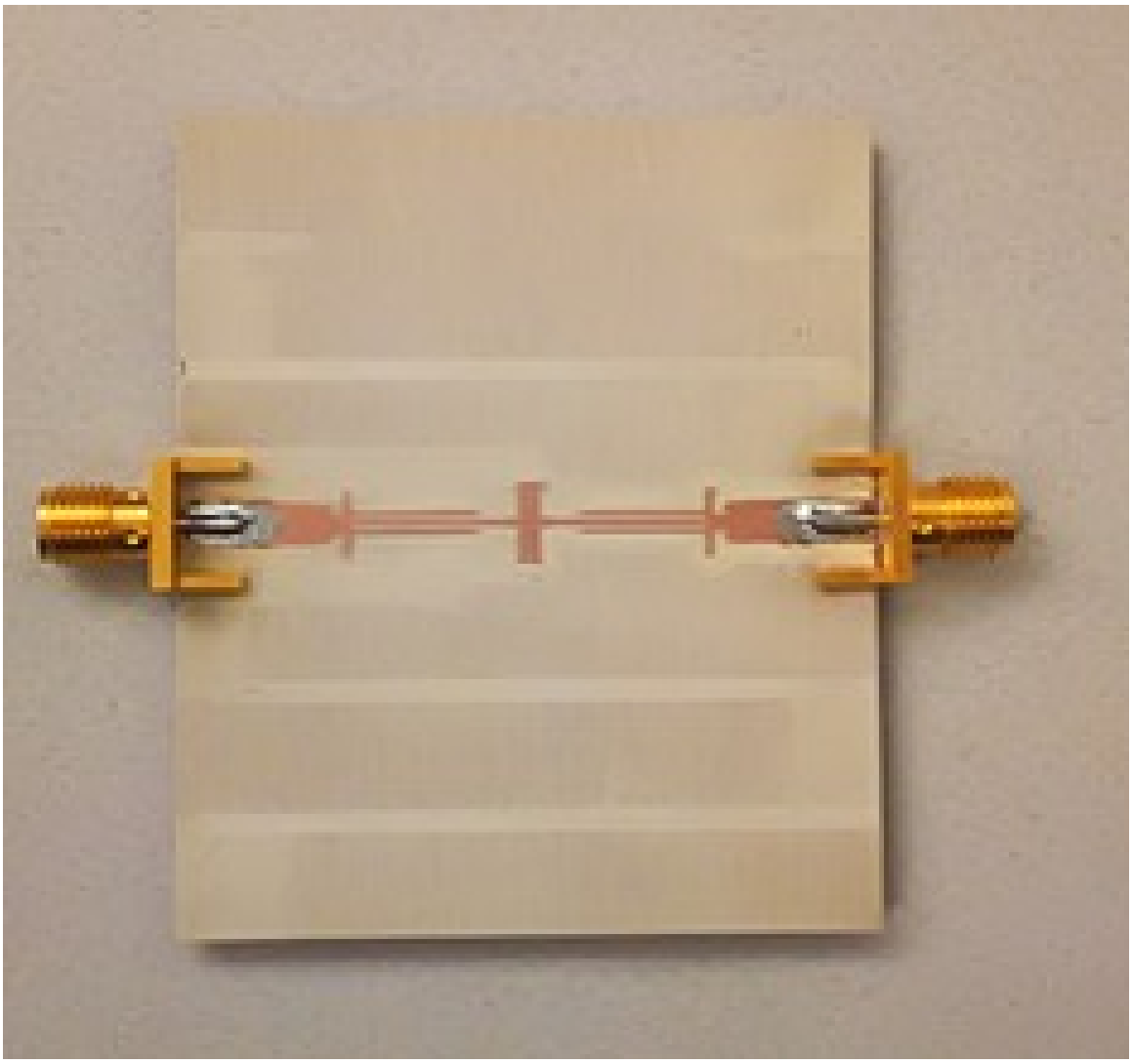

Figure 4.17: View of the fabricated proposed filter.

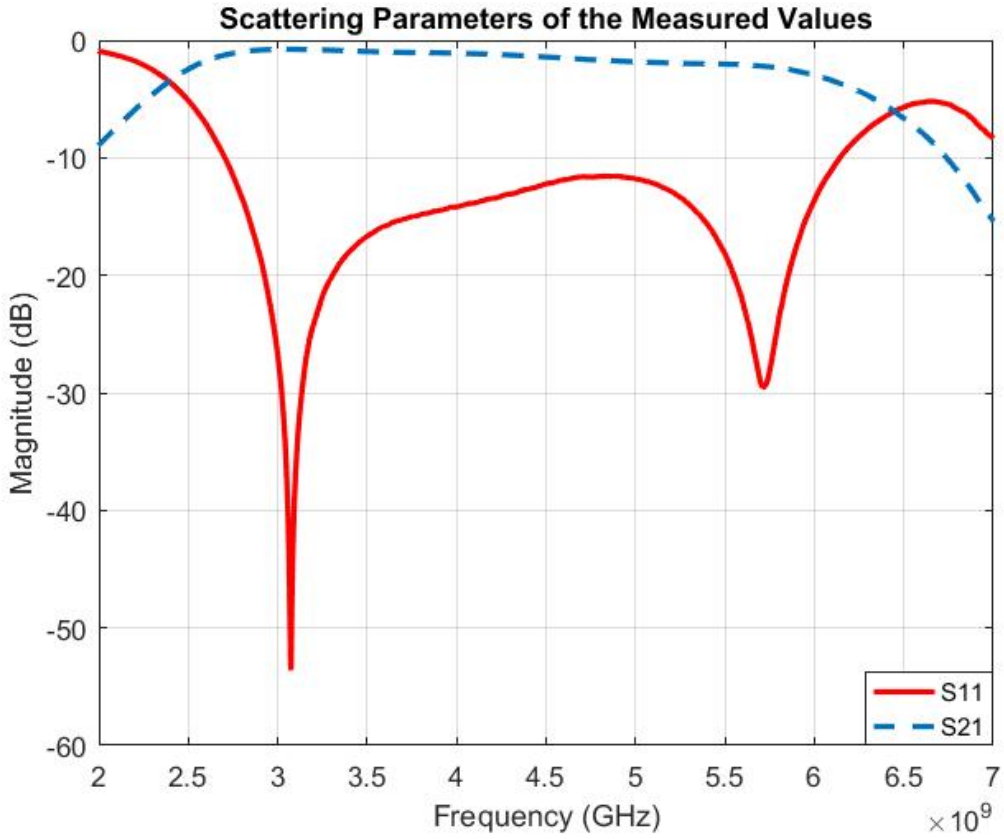

Figure 4.18: Scattering parameters of the fabricated filter.

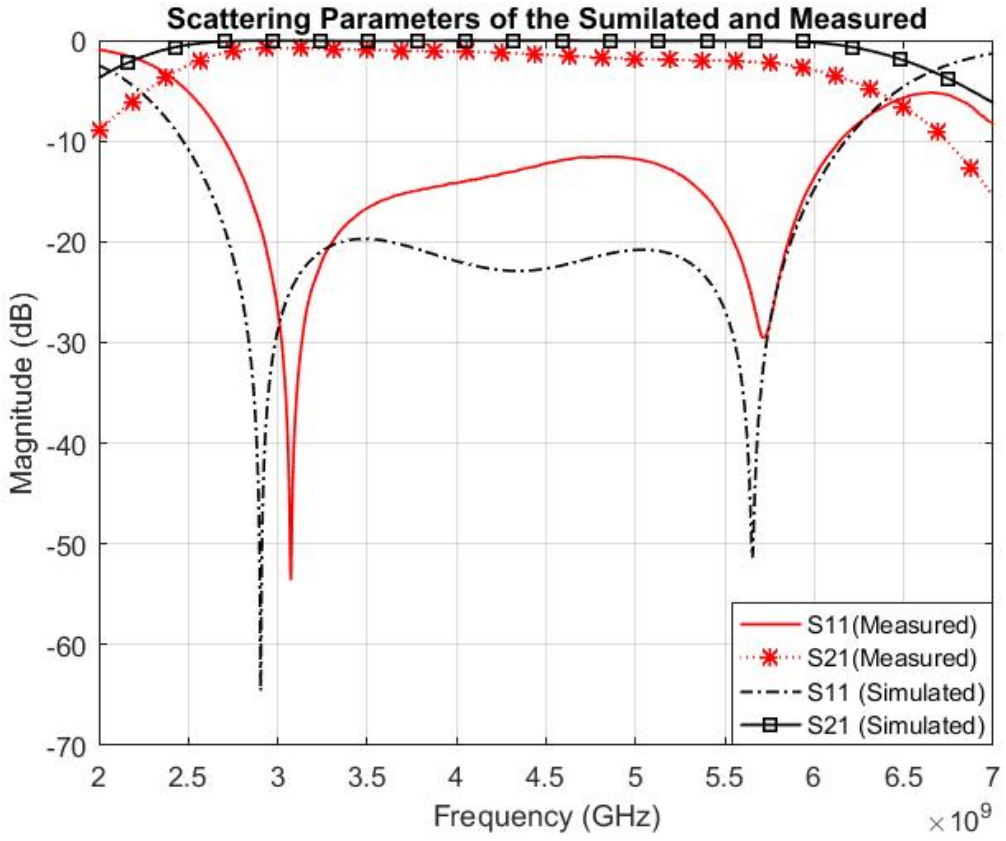

Figure 4.19: Scattering parameters of the simulated and measured values.

Chapter 5

Controlling Circuit Design

5.1 Introduction

In the previous chapter, we discussed the pre-filtering stage which is the first step of the energy detection technique. In this chapter, we present the circuit implementation of the proposed controlling system. We present the three Printed Circuit Boards (PCBs) that are used to apply the energy detection technique and we point out the advantages of RMS and Envelope Threshold Detection board (ADL 5904). Also. we present the micro-controller (ATmega328) and dual full bridge driver (L298) which are open-sources hardware. The two DC voltage outputs of the dual full bridge driver are connected to the power connector of the waveguide switch (WR229). The micro-controller uses the dual full bridge driver to set the suitable direction of the waveguide switch depending on the digital control output coming from the rms and envelope threshold detection.

5.2 Envelope Threshold Detection

In the market, there are several PCBs which are used to detect the presence or the absence of a signal over a specific bandwidth, such as: envelope and TruPwr rms detector (ADL 5511), envelope threshold detector (ADL 5910), and rms and envelope threshold detection (ADL 5904). The ADL 5511 has a RF input range of 45 dB, and supports up to 7 GHz. But, it has a high computational cost and operates at 5.25 V and 21.5 mA. Thus, it requires more power than the other PCBs to function [64]. The ADL 5910 supports up to 7 GHz and has a fast response time (12 ns). However, it has a RF input range of 40 dB [65].

Furthermore, we found out that the most suitable PCB for our proposed system is the rms and envelope threshold detection board (ADL 5904). The advantages of this detector are: it has a RF input range of 45 dB, from -30 dBm to 15 dBm, operates at 3.3 V and 3.5 mA, has a fast time response (12 ns), has a programmable envelope threshold detection function, it supports up to 7 GHz, and it has a Set-Reset (SR) flip-flop which is used to produce digital control output [66]. Figure 5.1 illustrates the block diagram of the rms and envelope threshold detection board.

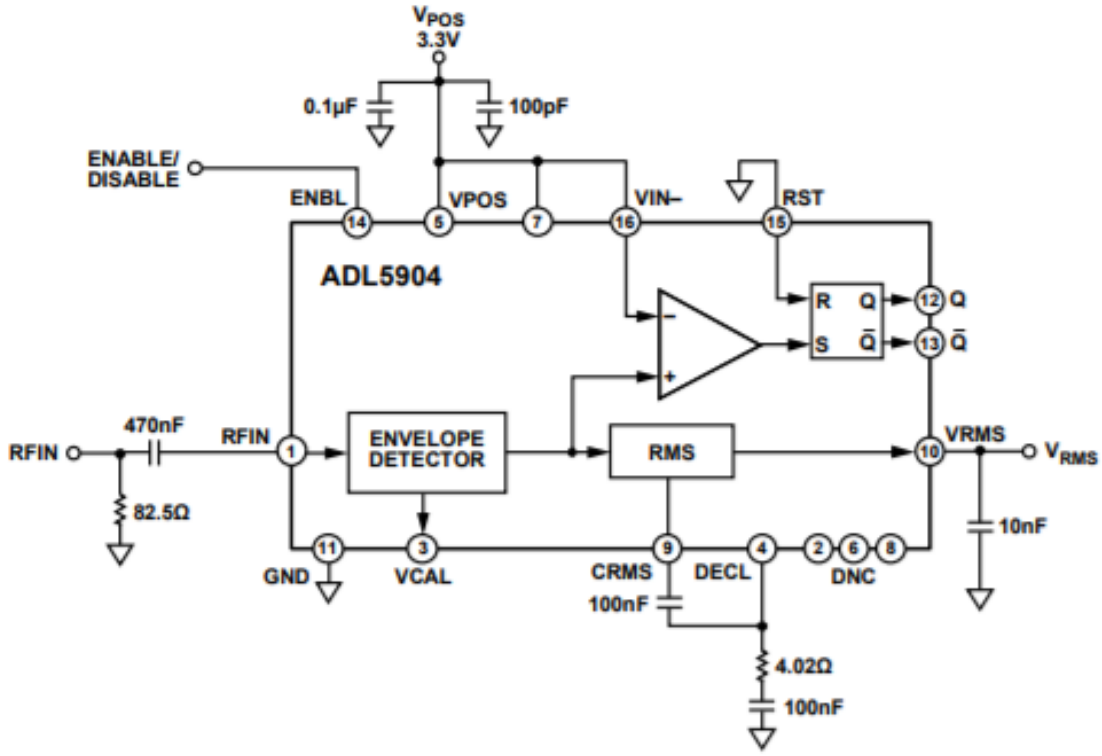

Figure 5.1: Block diagram of the rms and envelope threshold detection board [66].

The rms and envelope threshold detection board (ADL 5904) receives the RF filtered signal and produces digital control output from the SR flip-flop. The suitable threshold (VIN-) can be obtained by two steps. The first step is to measure the voltage at VCAL (Threshold Calibration) without applying a RF signal, where the voltage at VCAL is approximately 750 mV. The second step is to apply a RF signal and measure the voltage at VCAL. The difference between these two voltages is the desired threshold which will be applied to VIN-. Alternatively, there is a table of the recommended values for the threshold voltages over various frequencies [66]. The envelop detector measures the energy of the RF signal.

The presence or the absence of the signal can be known by comparing the energy of the RF signal with the threshold (VIN-). As shown in Fig. 5.1, when the energy of the RF signal exceeds the threshold (signal is present), the Q output of the SR flip-flop flips from logic low to high. On the other hand, the Q output of the SR flip-flop flips to logic low when the energy is less than the threshold (signal is absent). The Q output of the SR flip-flop is the digital control output that will be passed to the micro-controller. Figure 5.2 illustrates the schematic of the rms and envelop threshold detection board.

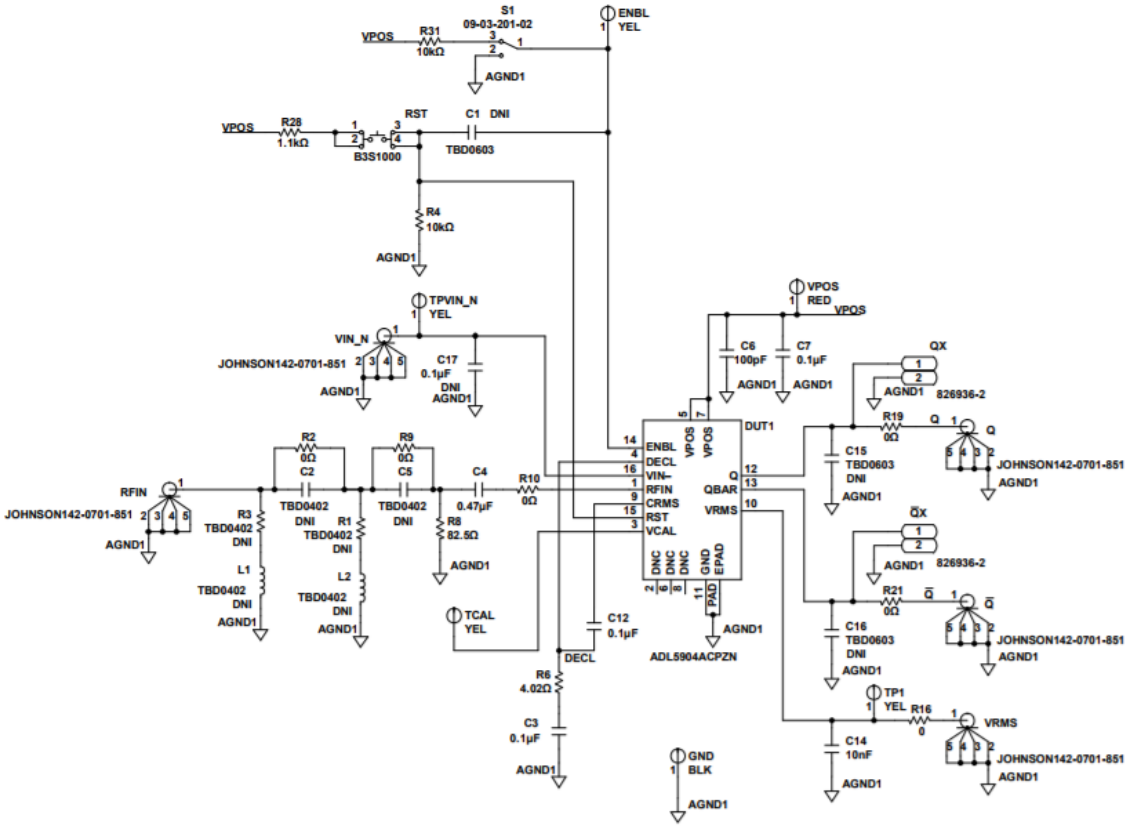

Figure 5.2: Schematic of the rms and envelope threshold detection board [66].

Figure 5.3 [66] (a) illustrates the response of the Q output of the SR flip-flop at 900 MHz, when the power of the RF signal ($P_{IN} = -5$ dBm) exceeds the threshold ($V = -10$ dBm) by 5 dB. The vertical line represents the beginning of the RF signal when its power exceeds the threshold power. Moreover, the time response that the Q output needs to change from logic low to high is approximately 12 ns. Figure 5.3 (b) shows the response of the Q output of the SR flip-flop, when the power of the RF signal ($P_{IN} = -9$ dBm) exceeds the threshold ($V = -10$ dBm) by 1 dB at the same frequency, and the time response is approximately 12

ns. Therefore, the time response of the Q output is irrelevant to how far the power of the RF signal exceeds the threshold power.

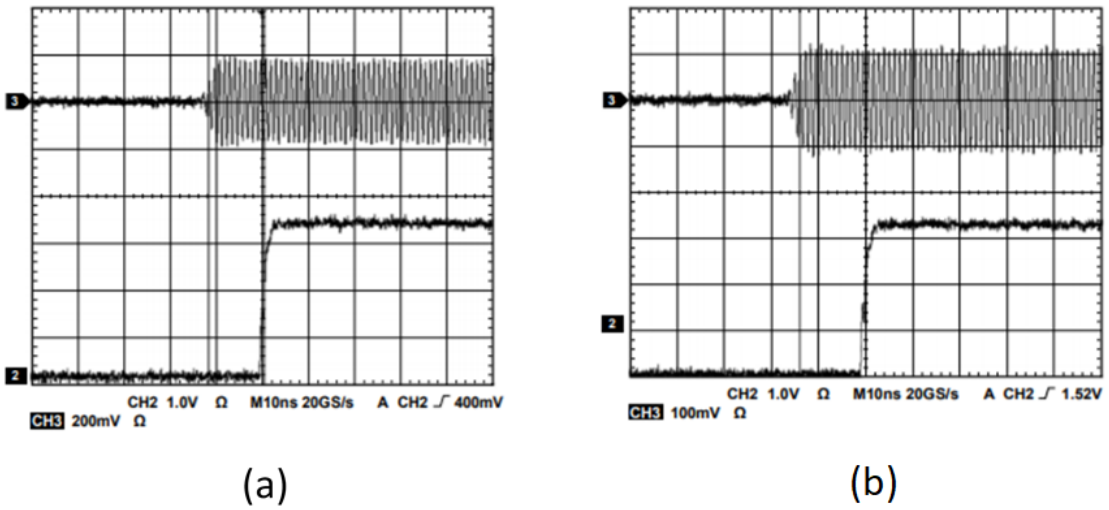

Figure 5.3: the response of the Q output [66] (a) the power of the RF signal exceeds the threshold by 5 dB (b) the power of the RF signal exceeds the threshold by 1 dB.

The latched event is held on the SR flip-flop until a reset pulse is applied. Hence, we programmed it to take a sample continuously over a specific time slot.

5.3 Micro-controller

The digital control output coming from the SR flip-flop (rms and envelope threshold detection board) is passed to the micro-controller (ATmega328) to control the direction of the waveguide switch via the dual full-bridge driver (L298). 8-bit AVR microcontroller is the family of the ATmega328, where it provides high performance. Table 5.1 shows the specifications of the ATmega328 [67]. It has an operating voltage range between 1.8 V to 5 V, clock speed of 16 MHz which means it samples the digital control data 16×10^6 samples, and it has a memory (Flash type) of 32 KB. Atmega328 can be programmed by using Arduino Software (IDE). ATmega328 is programmed to use the dual full-bridge driver (L298) to choose the suitable direction of the waveguide switch depending on the digital control output coming from the rms and envelope threshold detection [67]. Figure 5.4 illustrates the schematic of the ATmega328.

Table 5.1: Specifications of ATmega328.

Micro-controller	ATmega328
Architecture	AVR
Operating Voltage Range	1.8 V to 5 V
Flash Memory	32 KB
SRAM	2 KB
Clock Speed	16 MHz
Analog IN Pins	8
EEPROM	1 KB
Digital I/O Pins	22
Power Consumption	19 mA
Temperature Range	$-40°$C to $105°$C

Dual full-bridge driver (L298) is an integrated monolithic circuit in a 15-lead Multiwatt (L298N & L198HN) and PowerSO20 (L298P) packages. Figure 5.5 illustrates the block diagram of the dual full-bridge driver. Dual full-bridge driver has two separate power connections: one for the logic, and the other one is for the motor supply driver. Therefore it requires an external power supply (battery). It gives us the ability to drive two DC voltage outputs, where these DC voltage outputs are connected to the waveguide switch to change the direction of the switch [68]. Figure 5.6 presents the schematic of the dual full-bridge driver.

5.4 Waveguide Switches

Waveguide switches are electromagnetic switches with hollow circular or rectangular cross-sections. They are used to direct the path of the RF energy in microwave communications and radar applications. There are two types of waveguide switches, namely: Rectangular waveguide switches (RW), and Double-ridge waveguide switches (DW). The switch that is used in the system is a rectangular waveguide switch (WR229) [69]. Figure 5.7 depicts the dimensions of the waveguide switch (WR229) [70]. The waveguide switch (WR229) can be controlled manually or electrically by a power connector. Figure 5.8 is the block diagram of the power connector in the waveguide switch (WR229).

In our system, the rms and envelope threshold detection (ADL 5904) sends its output signal to the micro-controller (ATmega329) which is connected to the dual full bridge driver (L298). The dual full bridge driver has two DC voltage outputs connected to the power

connector (pins A & C) of the waveguide switch (WR229) which consists of two coils and a magnet. In the case the output of the dual full bridge driver is a high voltage DC signal, the coil connected to pin A is excited and generates a magnetic field which attracts the magnet and indicates the output direction of the waveguide switch. The opposite occurs in case of a logic low DC signal.

5.5 Summary

In this chapter, we addressed the circuit implementation of the proposed controlling system. We presented several Printed Circuit Boards (PCBs) applying the energy detection technique. We discussed the reasons for choosing the rms and envelope threshold detection board (ADL 5904). We addressed the specifications of the micro-controller (ATmega329) and the dual full bridge driver (L298). We presented how the waveguide switch can be controlled electrically.

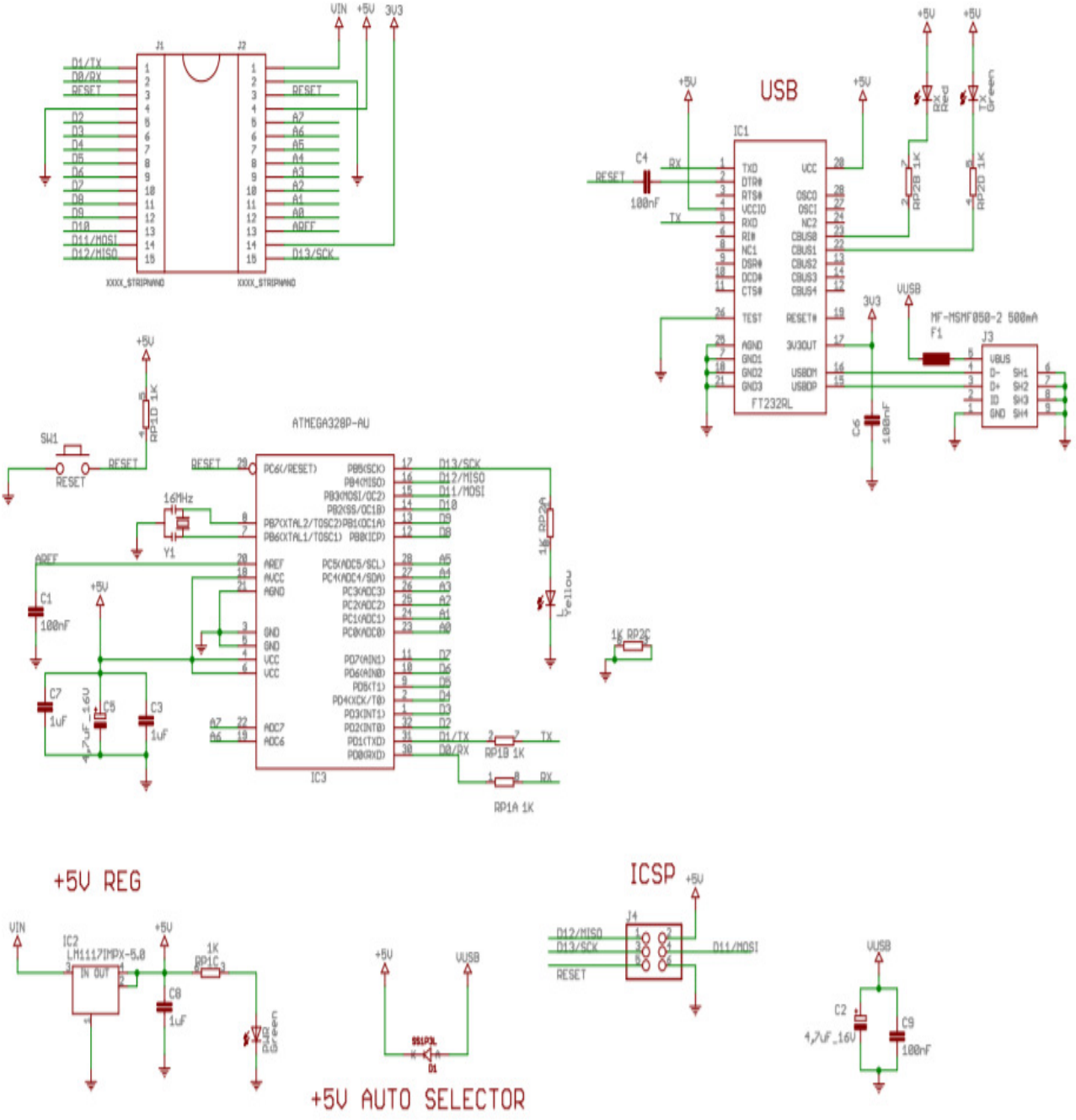

Figure 5.4: Schematic of the ATmega328 [67].

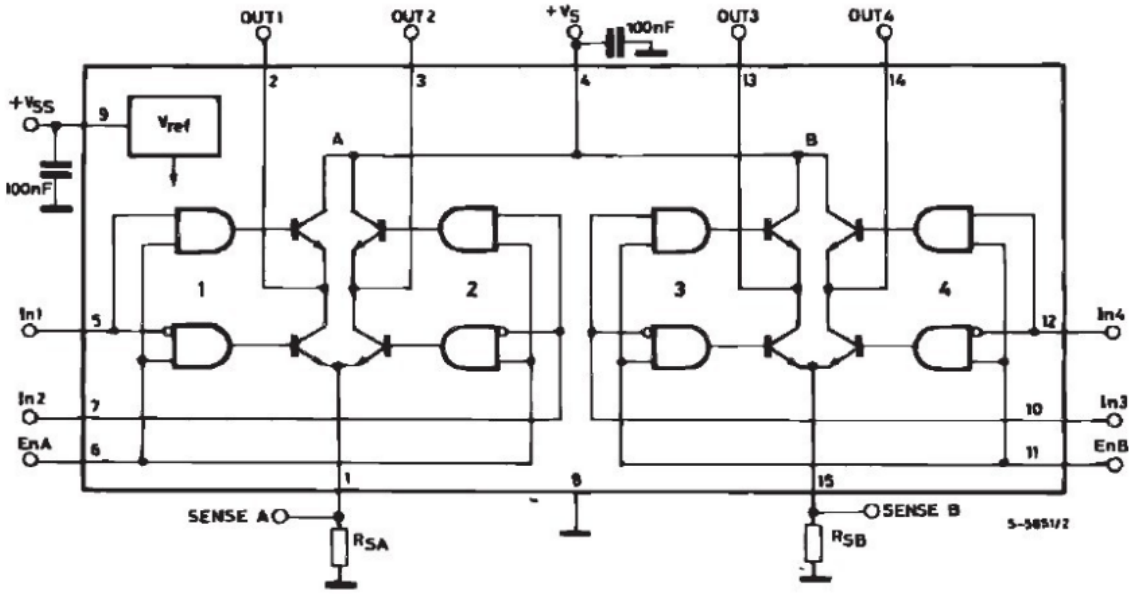

Figure 5.5: Block diagram of the dual full-bridge driver [68].

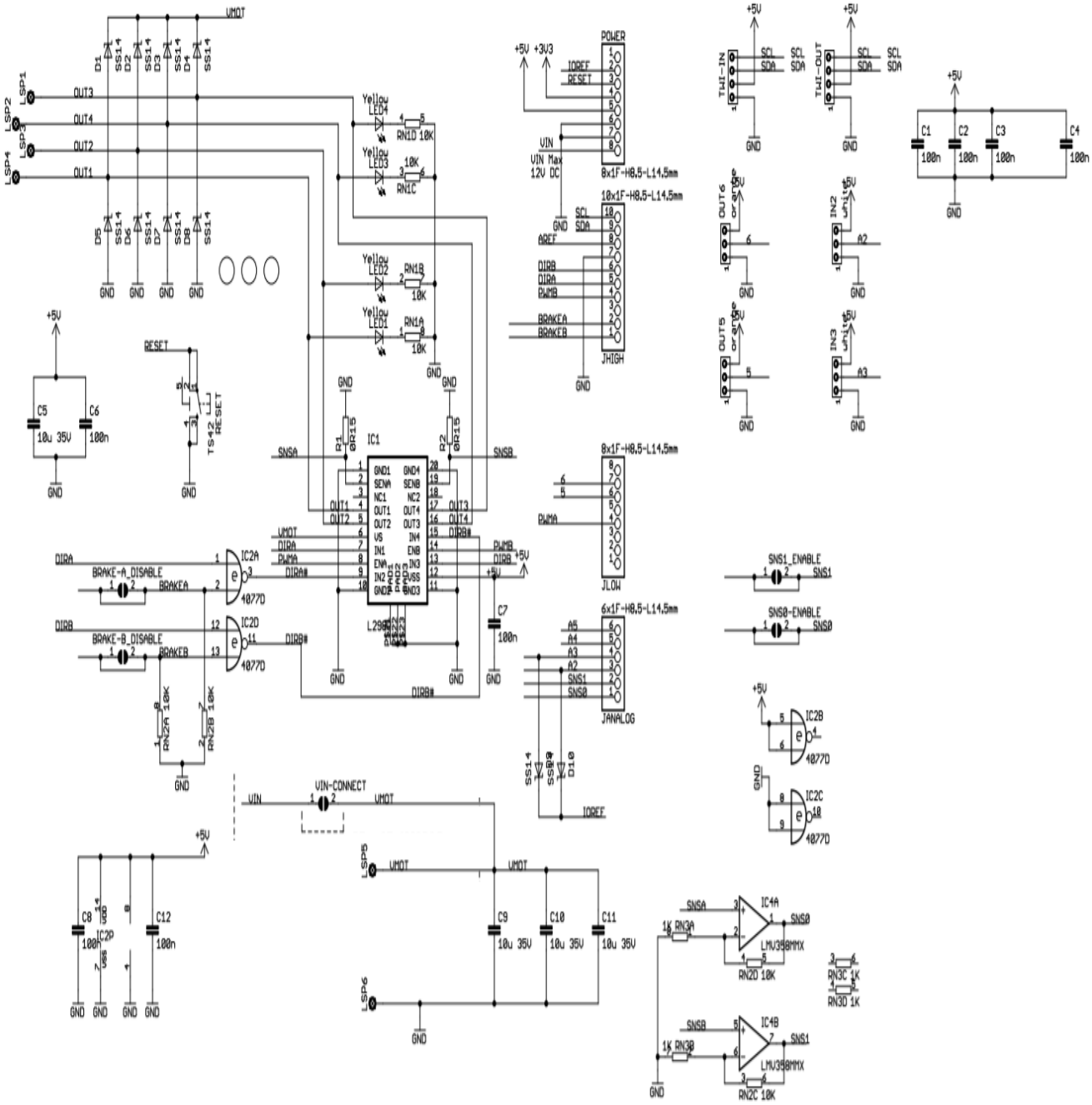

Figure 5.6: Schematic of the dual full-bridge driver [68].

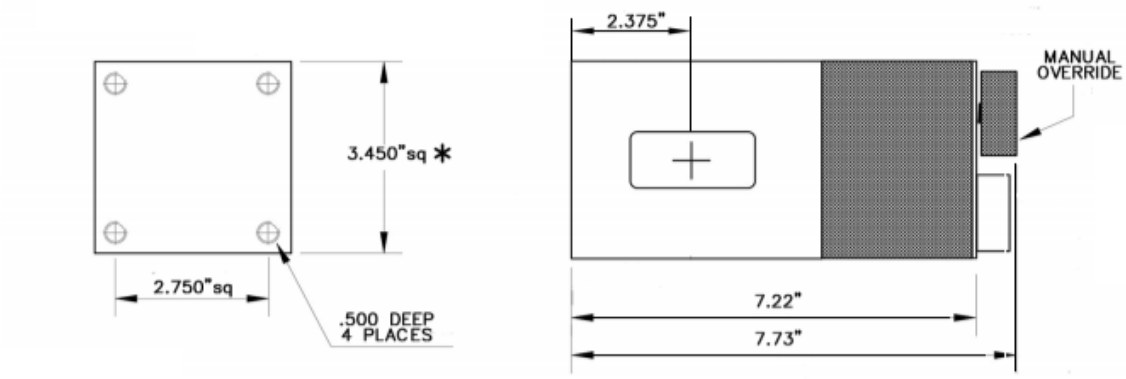

Figure 5.7: Dimensions of the waveguide switch (WR229) [70].

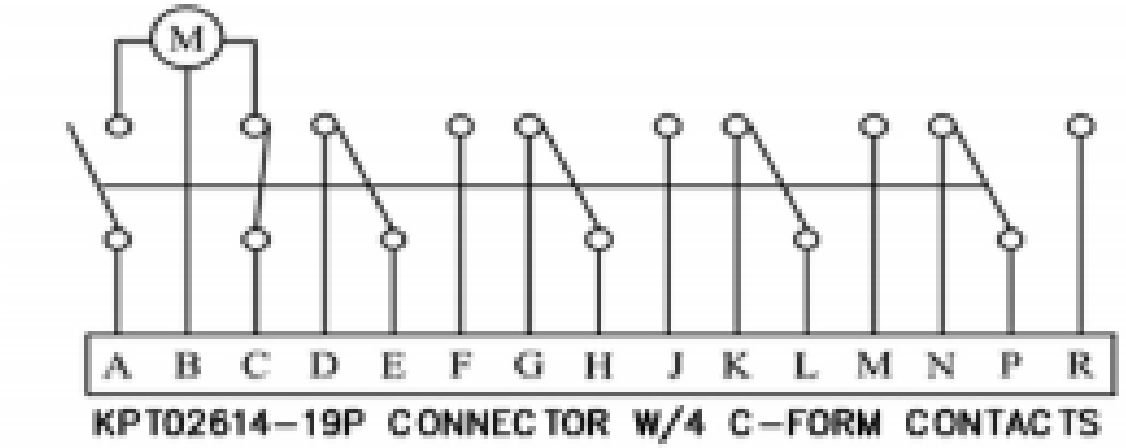

Figure 5.8: Block diagram of the power connector in the waveguide switch (WR229) [70].

Chapter 6

Performance of Energy Detectors

6.1 Introduction

The knowledge of the signal and noise characteristics is essential for signal detection in the presence of noise. For instance, if the form of the signal is known and the noise is Gaussian, the matched filter detection method is the most efficient technique in this situation. On the other hand, the signal is considered as a sample function of a random process, if the signal has an unknown form. Moreover, energy detection technique is the most suitable method in case of the absence of prior knowledge of the primary signal. In this chapter, we present the performance of the energy detector in the presence of noise in the base-band and the pass-band. Further, we propose using the Rayleigh channel model to emulate the behaviour of the coupling structure used to extract the RF signal sample from the wave-guiding structure. Hence, we present the performance of the energy detector over such environment in terms of receiver operating characteristic (ROC) curves.

6.2 Hypotheses Testing

There are two Hypotheses in the energy detection, namely: Hypothesis (H_0) and Hypothesis (H_1). Furthermore, H_0 represents the absence of the signal. In other words, the received signal contains the noise only as given in (6.1). On the other hand, H_1 represents the presence of the signal which consists of the primary signal and the noise as illustrated in (6.1)

$$\begin{aligned} H_0 &: y(t) = n(t) \\ H_1 &: y(t) = s(t) + n(t), \end{aligned} \tag{6.1}$$

where $y(t)$ represents the received signal, $n(t)$ is the noise waveform, and $n(t)$ is the signal waveform.

6.3 Detection in White Noise: Base-band Process

It is well known that the minimum time-bandwidth product of process within a time duration T and bandwidth W is given by $2TW$. The sampling rate of base-band and band-pass processes are $1/2W$ and $1/W$ [71], respectively. For the base-band noise random process, each sample of noise may be written as [72],

$$n(t) = \sum_{i=-\infty}^{\infty} a_i \; sinc(2Wt - i), \tag{6.2}$$

where $a_i = n(i/2W)$ is the noise sample value, i is the number of samples, and $sinc(x) = sin\pi x/\pi x$. It is noticeable that each a_i is a Gaussian random variable with zero mean and variance σ^2. Hence, $n(t)$ has the same variance as a_i, for example,

$$\sigma_i^2 = 2N_{02}W, \quad all \; i, \tag{6.3}$$

while N_{02} represents the two-sided noise power density spectrum. Using

$$\begin{aligned} \int_{-\infty}^{\infty} sinc(2Wt - i) \; sinc(2Wt - k) \; dt = 1/2W, \quad i = k \\ = 0. \qquad i \neq k \end{aligned} \tag{6.4}$$

It is possible to write

$$\int_{-\infty}^{\infty} n^2(t) \; dt = (1/2W) \sum_{i=-\infty}^{\infty} a_i^2. \tag{6.5}$$

Further, $n(t)$ may be approximated by a sum of $2TW$ terms over the interval $(0, T)$

$$n(t) = \sum_{i=1}^{2TW} a_i \; sinc(2Wt - i), \qquad 0 \; < \; t \; < \; T \tag{6.6}$$

Similarly, by using $2TW$ terms of the right-hand side of (6.6), the energy in a sample duration T may be approximated as [71]

$$\int_0^T n^2(t) \; dt = (1/2W) \sum_{i=1}^{2TW} a_i^2. \tag{6.7}$$

The reason for taking $2TW$ terms, that it is sufficient to approximate the energy in a limited duration sample of a band-limited process with having a flat power density spectrum is given by the Karhunen-Loeve expansion [73, p. 96]. If the noise signal $n(t)$ is a zero mean Gaussian stationary random process, and having a flat power density spectrum in $(-W, W)$, then its autocorrelation function R(τ) is given by [71]

$$R(\tau) = sinc(2W\tau). \tag{6.8}$$

By using the expansion of orthonormal functions $\phi_i(t)$, $n(t)$ may be re-written over the interval $(0, T)$ as:

$$n(t) = \sum_{i=1}^{\infty} \eta_i \phi_i(t), \tag{6.9}$$

where $\eta_i = \int_0^T n(t)\phi_i(t)dt$. After a certain index, how rapidly the eigenvalues decrease in value is what the number of terms in (6.9) depends on in order to get a good approximation with a finite number of terms. The $\phi_i(t)$ are eigenfunctions of the integral equation [71]

$$\int_0^T R\left(t-\tau\right)\phi_i(\tau)dt = g_i\phi_i(t), \tag{6.10}$$

where g_i represents the eigenvalues of the equation. It has been shown that, the eigenvalues after $2TW$ terms drop off rapidly, except when $TW = 1$. Thus, (6.9) is approximated by the sum of $2TW$ terms [71]

$$n(t) \simeq \sum_{i=1}^{2TW} \eta_i \phi_i(t). \tag{6.11}$$

The approximation (6.11) is more satisfactory than the approximation (6.6). By using (6.11) and the fact that $\phi_i(t)$ are orthonormal, the energy of the $n(t)$ over the interval $(0, T)$ can be approximated by [71]

$$\int_0^T n^2(t) \simeq \sum_{i}^{2TW} \eta_i^2. \tag{6.12}$$

In (6.12), η_i is Gaussian, since the process is Gaussian. While the variance of η_i is the eigenvalues (g_i) which are almost the same for $i \leq 2TW$. Therefore, the energy is the sum of $2TW$ squares of zero mean Gaussian variates with the same variance, which led to the chi-square distribution (X_k^2) by the convenient normalization [71]. The normalized test statistic $V^{'}$ is expressed in the form [71]

$$V^{'} = (1/N_{02}) \int_0^T y^2(t)\, dt, \tag{6.13}$$

by comparing between (6.7) and (6.13), it is obvious that (6.7) is $N_{02}V^{'}$, where $V^{'}$ is the normalized test statistic under H_0 (signal is absent). The normalized noise sample value b_i can be written as [71]

$$b_i = a_i/\sqrt{2WN_{02}}, \tag{6.14}$$

the test statistic under H_0 can be expressed as [71]

$$V^{'} = \sum_{i=1}^{2TW} b_i^2. \tag{6.15}$$

Consequently, the decision statistic under H_0 is the sum of the squares of $2TW$ Gaussian random variables, where each b_i has a zero mean and unit variance $[V^{'} \sim N(0,1)]$. Thus, $V^{'}$ has a chi-square distribution with $2TW$ degrees of freedom, which are provided in tables [74]-[76]. Under H_1, where the signal is present, by using the finite sum of $2TW$, the signal of duration T may be written as

$$s(t) = \sum_{i=1}^{2TW} \alpha_i \; sinc(2Wt - i), \tag{6.16}$$

where α_i is signal sample value

$$\alpha_i = s(i/2W). \tag{6.17}$$

The signal energy over the interval $(0, T)$, may be approximated by

$$\int_0^T s^2(t)\, dt = (1/2W) \sum_{i=1}^{2TW} \alpha_i^2. \tag{6.18}$$

Defining the normalized signal sample value β_i

$$\beta_i = \alpha_i/\sqrt{2WN_{02}}, \tag{6.19}$$

by substituting (6.19) in (6.18), it can be written

$$(1/N_{02}) \int_0^T s^2(t)\, dt = \sum_{i=1}^{2TW} \beta_i^2. \tag{6.20}$$

By using (6.2) and (6.16), the received signal $y(t)$ when the signal is present may be represented as:

$$y(t) = \sum_{i=1}^{2TW} (a_i + \alpha_i) \; sinc(2Wt - i). \tag{6.21}$$

The energy of the received signal over the interval $(0, T)$ can be illustrated as:

$$\int_0^T y^2(t)\, dt = (1/2W) \sum_{i=1}^{2TW} (a_i + \alpha_i)^2. \tag{6.22}$$

The normalized test statistic under H_1 is

$$V^{'} = (1/N_{02}) \int_0^T y_t^2\, dt = \sum_{i=1}^{2TW} (b_i + \beta_i)^2. \tag{6.23}$$

We deduce from (6.23) that the normalized test statistic under H_1 has a noncentral chi-square distribution ($X_k^2(\lambda)$) with $2TW$ degrees of freedom and a noncentrality parameter (λ) [77], [78]

$$\lambda = \sum_{i=1}^{2TW} \beta_i^2 = (1/N_{02}) \int_0^T s^2(t)\, dt = E_s/N_{02}, \tag{6.24}$$

where E_s is the signal energy and λ represents the signal-to-noise ratio (SNR). Extensive tables do not exist for noncentral chi-square distribution, therefore approximations have been used instead.

6.4 Detection in White Noise: Band-pass Process

In a band-pass random process, every sample function can be written as [73]

$$n(t) = n_c(t)\, cos(w_c t) - n_s(t)\, sin(w_c t), \tag{6.25}$$

where $n_c(t)$ represents the in-phase component of the $n(t)$, while $n_s(t)$ is the quadrature component of the $n(t)$. Further, $n_c(t)$ and $n_s(t)$ have flat power density spectrum, where each one is equal to $2N_{02}$ over the band $\mid f \mid < W/2$. Hence, each of the in-phase and quadrature components have TW degrees of freedom with variance ($\sigma^2 = 2N_{02}W$). Moreover, when T increases, it is possible to achieve a good approximation as shown below,

$$\int_0^T n^2(t)\, dt = \frac{1}{2} \int_0^T [n_c^2(t) + n_s^2(t)]\, dt. \tag{6.26}$$

The energy in $n_c(t)$ and $n_s(t)$ may be found similar to the previous section

$$\begin{aligned} \int_0^T n_c^2(t)\, dt &= (1/W) \sum_{i=1}^{TW} a_{ci}^2 \\ \int_0^T n_s^2(t)\, dt &= (1/W) \sum_{i=1}^{TW} a_{si}^2, \end{aligned} \tag{6.27}$$

where a_{ci}^2 and a_{si}^2 are the noise sample value of the in-phase and quadrature modulation, respectively. Using

$$\begin{aligned} a_{ci} &= n_c(i/W) \\ a_{si} &= n_s(i/W). \end{aligned} \tag{6.28}$$

The normalized noise sample value of the in-phase sample value b_{ci} and the normalized noise sample value of the quadrature sample value b_{si} can be written as:

$$\begin{aligned} b_{ci} &= a_{ci}/\sqrt{2WN_{02}} \\ b_{si} &= a_{si}/\sqrt{2WN_{02}}. \end{aligned} \tag{6.29}$$

Therefore, the normalized test statistic under H_0 is

$$V^{'} = (1/N_{02}) \int_0^T n^2(t)\, dt = \sum_{i=1}^{TW} (b_{ci}^2 + b_{si}^2), \tag{6.30}$$

where any b_{ci} or b_{si} has a unity variance. Thus, the normalized decision statistic under H_0 has a chi-square distribution with $2TW$ degrees of freedom.
The expression of the band-pass signal is

$$s(t) = s_c(t)\ cos(w_c t) - s_s(t)\ sin(w_c t), \tag{6.31}$$

where $s_c(t)$ and $s_s(t)$ have frequency component over the region $\mid f \mid < W/2$. As before

$$\begin{aligned} s_c(t) &= \sum_{i=1}^{TW} \alpha_{ci}\ sinc(Wt - i) \\ s_s(t) &= \sum_{i=1}^{TW} \alpha_{si}\ sinc(Wt - i), \end{aligned} \tag{6.32}$$

where

$$\begin{aligned} \alpha_{ci} &= s_c(i/W) \\ \alpha_{si} &= s_s(i/W). \end{aligned} \tag{6.33}$$

So, the received signal $y(t)$ may be derived

$$\begin{aligned} y(t) &= [s_c(t) + n_c(t)]\ cos(w_c t) - [s_s(t) + n_s(t)]\ sin(w_c t) \\ &= y_c(t)\ cos(w_c t) - y_s(t)\ sin(w_c t), \end{aligned} \tag{6.34}$$

where $y_c(t)$ and $y_s(t)$ can be written as

$$\begin{aligned} y_c(t) &= s_c(t) + n_c(t) = (1/W) \sum_{i=1}^{TW} (\alpha_{ci} + a_{ci})\ sinc(Wt - i) \\ y_s(t) &= s_s(t) + n_s(t) = (1/W) \sum_{i=1}^{TW} (\alpha_{si} + a_{si})\ sinc(Wt - i), \end{aligned} \tag{6.35}$$

while

$$\begin{aligned} \beta_{ci} &= s_c(i/W)\sqrt{2WN_{02}} \\ \beta_{si} &= s_s(i/W)\sqrt{2WN_{02}}, \end{aligned} \tag{6.36}$$

where β_{ci} and β_{si} are the normalized signal sample value of in-phase and quadrature components, respectively. So, by following the same logic as before

$$(1/N_{02}) \int_0^T s^2(t)\ dt = \sum_{i=1}^{TW} (\beta_{ci}^2 + \beta_{si}^2) = E_s/N_{02}. \tag{6.37}$$

Thus, under H_1 (signal is present), the energy of the received signal is

$$\begin{aligned} \int_0^T y^2(t) &= \frac{1}{2} \int_0^T [y_c^2(t) + y_s^2(t)] dt \\ &= \frac{1}{2} \int_0^T [s_c(t) + n_c(t)]^2 dt \\ &\quad + \frac{1}{2} \int_0^T [s_s(t) + n_s(t)]^2 dt. \end{aligned} \tag{6.38}$$

The normalized test statistic $V^{'}$ under H_1 may be written by using (6.20), (6.23), (6.37), and (6.38)

$$V^{'} = \sum_{i=1}^{TW} [(b_{ci} + \beta_{ci})^2 + (b_{si} + \beta_{si})^2] \tag{6.39}$$

It is obvious that $V^{'}$ has a noncentral chi-square distribution with 2TW degrees of freedom and a noncentrality parameter $\lambda = E_s/N_{02}$. Therefore, by comparing the results in the base-band process and band-pass process, one can conclude that both processes have the same decision statistics [71].

6.5 Probability of False Alarm and Probability of Detection

For a given threshold $V_T^{'}$, the probability of false alarm P_{fa} is, under H_0, defined by

$$P_{fa} = Prob\left(V^{'} > V_T^{'} \mid H_0\right) = Prob\left(X_{2TW}^2 > V_T^{'}\right), \tag{6.40}$$

where X_{2TW}^2 follows a chi-square distribution with $2TW$ degrees of freedom as we discussed in the previous section 6.3. On the other hand, the probability of detection P_d for the same given threshold $V_T^{'}$ is formulated as:

$$P_d = Prob\left(V^{'} > V_T^{'} \mid H_1\right) = Prob\left(X_{2TW}^2(\lambda) > V_T^{'}\right), \tag{6.41}$$

where $X_{2TW}^2(\lambda)$ represents a noncentral chi-square variable with $2TW$ degrees of freedom and noncentrality parameter $\lambda = E_s/N_{02}$.

As shown before, the noncentral chi-square has $2TW$ degrees of freedom and noncentrality parameter λ (defined as signal-to-noise ratio). The noncentral chi-square probabilities can be computed using the approximation of its probabilities by those of a central chi-square distribution which are tabulated. If we define the modified number of degrees of freedom D and the threshold divisor G by [71]:

$$\begin{aligned} D &= (2TW + \lambda)^2/(2TW + 2\lambda) \\ G &= (2TW + 2\lambda)/(2TW + \lambda). \end{aligned} \tag{6.42}$$

The right hand side of (6.41) can be approximated by the upper tail probability of the central chi-square distribution with D degrees of freedom as shown below:

$$Prob\left\{X_{2TW}^2(\lambda) > V_T^{'}\right\} = Prob\left\{X_D^2 > V_T^{'}/G\right\}. \tag{6.43}$$

Using (6.25) and (6.31), it can be shown that the squared envelope of the noise $n(t)$ is

$$Env^2[n(t)] = n_c^2 + n_s^2, \tag{6.44}$$

while the squared envelope of the signal $s(t)$

$$Env^2[s(t)] = s_c^2 + s_s^2. \tag{6.45}$$

Using (6.22), we can show that

$$a_{ci}^2 + a_{si}^2 = Env^2[n(i/W)], \tag{6.46}$$

and

$$b_{ci}^2 + b_{si}^2 = (1/2WN_{02})Env^2[n(i/W)], \tag{6.47}$$

by following the same approach as before

$$(b_{ci} + \beta_{ci})^2 + (b_{si} + \beta_{si})^2 = (1/2WN_{02})Env^2[s(i/W) + n(i/W)]. \tag{6.48}$$

Hence, when $TW = 1$ the normalized test statistic $V^{'}$ may be found by sampling at $t = T$ the squared envelope of the input to the energy detector. In this case, the conditional probability density functions of $V^{'}$ can be obtained in finite form and there are some difficulties in calculating the probability of detection. Based on the approximation of the envelope like the test statistic, the probability of false alarm and the probability of detection may be computed.

6.6 Probability of Detection and Probability of False Alarm over AWGN

The author in [71] presented an approximate expression for the probability of detection over AWGN while the authors in [79] showed exact closed-form for the probability of detection and the probability of false alarm.

Generally, the probability of detection and the probability of false alarm may be found by using (6.41) and (6.40), respectively. Further, according to the base-band or band-pass processes, the decision statistic $V^{'}$ may be described as [79]

$$V^{'} \sim \begin{cases} X_{2TW}^2, & H_0, \\ X_{2TW}^2(2\gamma), & H_1, \end{cases} \tag{6.49}$$

where $\gamma = \frac{E_s}{N_{01}}$ is the signal-to-noise ratio (SNR), which is equivalent to $\frac{\lambda}{2}$ in [71]. The probability density function $f(.)$ (PDF) of the decision statistic given as

$$f_{V'}(y) = \begin{cases} \frac{1}{2^u \Gamma(u)} y^{u-1} e^{-\frac{y}{2}}, & H_0, \\ \frac{1}{2}\left(\frac{y}{2\gamma}\right)^{\frac{u-1}{2}} e^{-\frac{2\gamma+y}{2}} I_{u-1}(\sqrt{2\gamma y}), & H_1, \end{cases} \tag{6.50}$$

where $u = TW$ is the time bandwidth product, $\Gamma(.)$ is the gamma function [80], and $I_n(.)$ is the nth-order modified Bessel function of the first kind [80]. Then, the probability of

false alarm P_{fa} can be obtained by using (6.50) [79] as:

$$P_{fa} = \frac{\Gamma(u, \frac{V_T^{'}}{2})}{\Gamma(u)}, \tag{6.51}$$

where $\Gamma(.,.)$ is the incomplete gamma function [80]. The probability of detection can be found by using (6.50) with the aid of [81, Eq. (2.1-124)], the cumulative distribution function $F(.)$ (CDF) of the test statistic $V^{'}$ is given by:

$$F_{V'}(y) = 1 - Q_u\left(\sqrt{2\gamma}, \sqrt{V_T^{'}}\right), \tag{6.52}$$

where $Q_u(a, b)$ is the generalized Marcum Q-function [82]. The probability of detection P_d may be obtained [71]

$$P_d = Q_u\left(\sqrt{2\gamma}, \sqrt{V_T^{'}}\right). \tag{6.53}$$

Receiver operating characteristic (ROC) curve [83] is used to present the performance of the energy detector which illustrates the relation between the probability of detection P_d versus the probability of false alarm P_{fa}. It is possible to plot the complementary ROC which represents the relation between the probability of miss detection P_m versus the probability of false alarm P_{fa}, where P_m may be obtained easily $(P_m = 1 - P_d)$. Figure 6.1 illustrates the performance of the energy detector over an AWGN channel, where the performance improves by increasing the number of samples when the signal-to-noise ratio is equal to -10 dB and the Number of iterations is 10^5.

6.7 Average Probability of Detection over Rayleigh Channel

The probability of false alarm P_{fa} over any fading channel is the same as (6.51) because it is considered in the hypothesis H_0 (when the signal is absent) and it is independent of SNR. On the other hand, the average probability of detection P_d may be obtained by averaging P_d in the AWGN case (6.53) over the SNR fading distribution. The SNR (γ) follows an exponential PDF, if the signal amplitude follows a Rayleigh distribution

$$f(\gamma) = \frac{1}{\overline{\gamma}}\, exp\left(-\frac{\gamma}{\overline{\gamma}}\right), \qquad \gamma \geq 0 \tag{6.54}$$

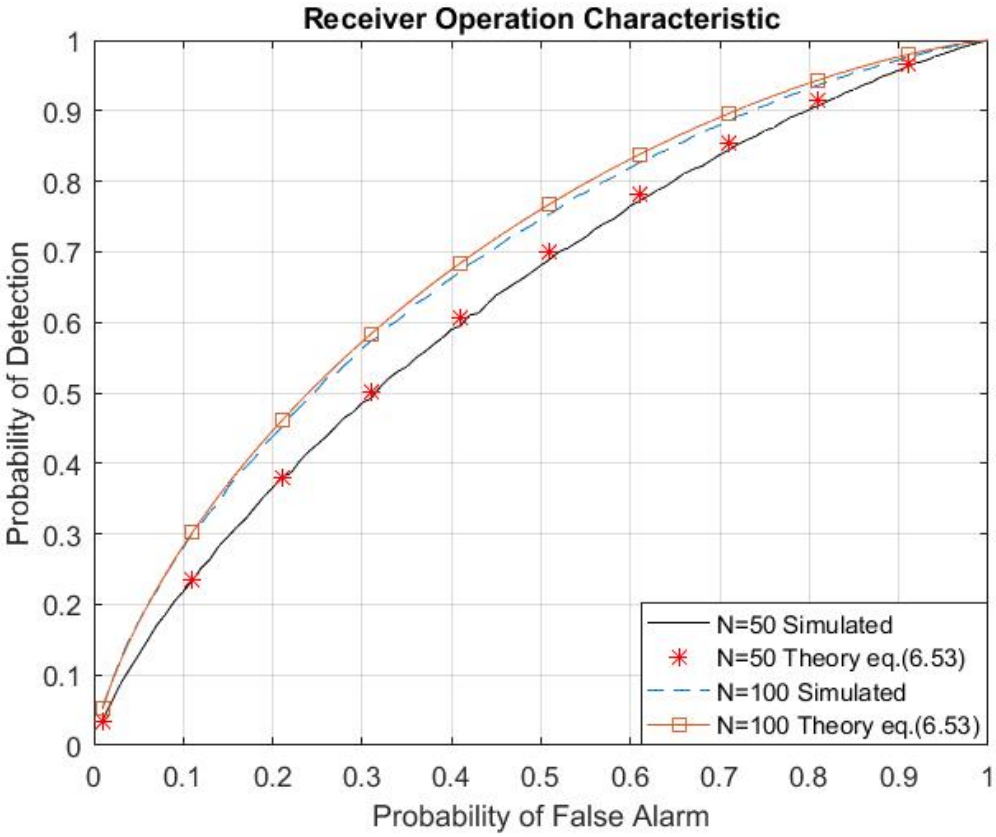

Figure 6.1: Performance of the energy detector over AWGN channel.

Now, the probability of detection over Rayleigh channel ($\overline{P_{dRay}}$) can be computed by averaging (6.53) over (6.54) with the aid of [82, Eq. (30)] and making the change of variable $x = \sqrt{2\gamma}$ [71], where [82, Eq. (30)] is given as

$$\int_0^\infty dx\; x\; exp\left(-\frac{p^2x^2}{2}\right) Q_M(ax,b) = \frac{1}{p^2} exp\left(-\frac{b^2}{2}\right) \left[\left(\frac{p^2+a^2}{a^2}\right)^{M-1}\left[exp\left(\frac{b^2}{2}\frac{a^2}{p^2+a^2}\right) - \sum_{n=0}^{M-2}\frac{1}{n!}\left(\frac{b^2}{2}\frac{a^2}{p^2+a^2}\right)^n\right] + \sum_{n=0}^{M-2}\frac{1}{n!}\left(\frac{b^2}{2}\right)^n\right], \tag{6.55}$$

where $p^2 = \frac{1}{\overline{\gamma}}$, $b = \sqrt{V_T^{'}}$, $M = u$, $a = 1$, and x is

$$x = \sqrt{2\gamma} \qquad d\gamma = x\; dx$$
$$x^2 = 2\gamma \qquad \frac{d\gamma}{x} = dx$$
$$\gamma = \frac{x^2}{2}$$

The $\overline{P_{dRay}}$ can be obtained using (6.55)

$$\overline{P_{dRay}} = \left(\frac{1}{\overline{\gamma}}\right)\overline{\gamma}\; exp\left(-\frac{V_T^{'}}{2}\right) \left[\left(\frac{\frac{1}{\overline{\gamma}}+1}{1}\right)^{u-1}\left[exp\left(\frac{V_T^{'}}{2}\frac{1}{\frac{1}{\overline{\gamma}}+1}\right) - \sum_{n=0}^{u-2}\frac{1}{n!}\left(\frac{V_T^{'}}{2}\frac{1}{\frac{1}{\overline{\gamma}}+1}\right)^n\right] + \sum_{n=0}^{u-2}\frac{1}{n!}\left(\frac{V_T^{'}}{2}\right)^n\right]$$
$$= e^{\left(-\frac{V_T^{'}}{2}\right)}\left[\left(\frac{1+\overline{\gamma}}{\overline{\gamma}}\right)^{u-1}\left[e^{\left(\frac{V_T^{'}\overline{\gamma}}{2(1+\overline{\gamma})}\right)} - \sum_{n=0}^{u-2}\frac{1}{n!}\left(\frac{V_T^{'}\overline{\gamma}}{2\,(1+\overline{\gamma})}\right)^n\right] + \sum_{n=0}^{u-2}\frac{1}{n!}\left(\frac{V_T^{'}}{2}\right)^n\right]$$
$$= e^{\left(-\frac{V_T^{'}}{2}\right)}\sum_{n=0}^{u-2}\frac{1}{n!}\left(\frac{V_T^{'}}{2}\right)^n + \left(\frac{1+\overline{\gamma}}{\overline{\gamma}}\right)^{u-1}\left[e^{\left(\frac{V_T^{'}}{2}\right)}e^{\left(\frac{V_T^{'}\overline{\gamma}}{2(1+\overline{\gamma})}\right)} - e^{\left(-\frac{V_T^{'}}{2}\right)}\sum_{n=0}^{u-2}\frac{1}{n!}\left(\frac{V_T^{'}\overline{\gamma}}{2\,(1+\overline{\gamma})}\right)^n\right]$$

where $e^{\left(\frac{V_T^{'}}{2}\right)}e^{\left(\frac{V_T^{'}\overline{\gamma}}{2(1+\overline{\gamma})}\right)}$ can be expressed as

$$e^{\left(\frac{V_T^{'}}{2}\right)}e^{\left(\frac{V_T^{'}\overline{\gamma}}{2(1+\overline{\gamma})}\right)} = e^{\left(\frac{-V_T^{'}}{2}+\frac{V_T^{'}\overline{\gamma}}{2+2\overline{\gamma}}\right)}$$
$$e^{\frac{-V_T^{'}(2+2\overline{\gamma})+2V_T^{'}\overline{\gamma}}{4+4\overline{\gamma}}} = e^{\frac{-2V_T^{'}-2V_T^{'}\overline{\gamma}+2V_T^{'}\overline{\gamma}}{4(1+\overline{\gamma})}}$$
$$e^{\frac{-2V_T^{'}}{4(1+\overline{\gamma})}} = e^{\frac{-V_T^{'}}{2(1+\overline{\gamma})}}$$

As a consequence, the average probability of detection over Rayleigh channel after the simplifications may be expressed as [79]

$$\overline{P_{dRay}} = e^{-\frac{V_T^{'}}{2}} \sum_{n=0}^{u-2} \frac{1}{n!} \left(\frac{V_T^{'}}{2}\right)^n \left(\frac{1+\overline{\gamma}}{\overline{\gamma}}\right)^{u-1} \left[e^{-\frac{V_T^{'}}{2(1+\overline{\gamma})}} - e^{-\frac{V_T^{'}}{2}} \sum_{n=0}^{u-2} \frac{1}{n!} \left(\frac{V_T^{'}\overline{\gamma}}{2(1+\overline{\gamma})}\right)^n\right]. \tag{6.56}$$

It is noticeable that (6.56) is equivalent to the one given in [84, Eq. (20)], by making some correlations and observations such as: expressing the normalized incomplete gamma function in its series form [80, Eq. (8.352.1)], assuming $d^2 = \overline{\gamma}$, replacing each B by $\frac{B}{2} - 1$, and inserting a minus sign in the exponential [71].

We assumed the performance of the system is over Rayleigh channel. Figure 6.2 illustrates ROC curve over Rayleigh channel with different number of samples (L). We observe that by increasing the number of samples, the performance is getting better over Rayleigh which makes sense because when the number of samples increases, it will detect more accurately. Our results were obtained when the signal-to-noise ratio is equal to 0 dB and the number of iterations is 10^5.

6.8 Summary

In this chapter, we addressed the hypotheses testing of the energy detection. We showed that the decision statistics in the base-band and band-pass processes are equivalent. We addressed the computation of the probability of false alarm and probability of detection when time-bandwidth product is small and large. Also, we presented the performance of the probability of false alarm and probability of detection over AWGN and Rayleigh fading channels.

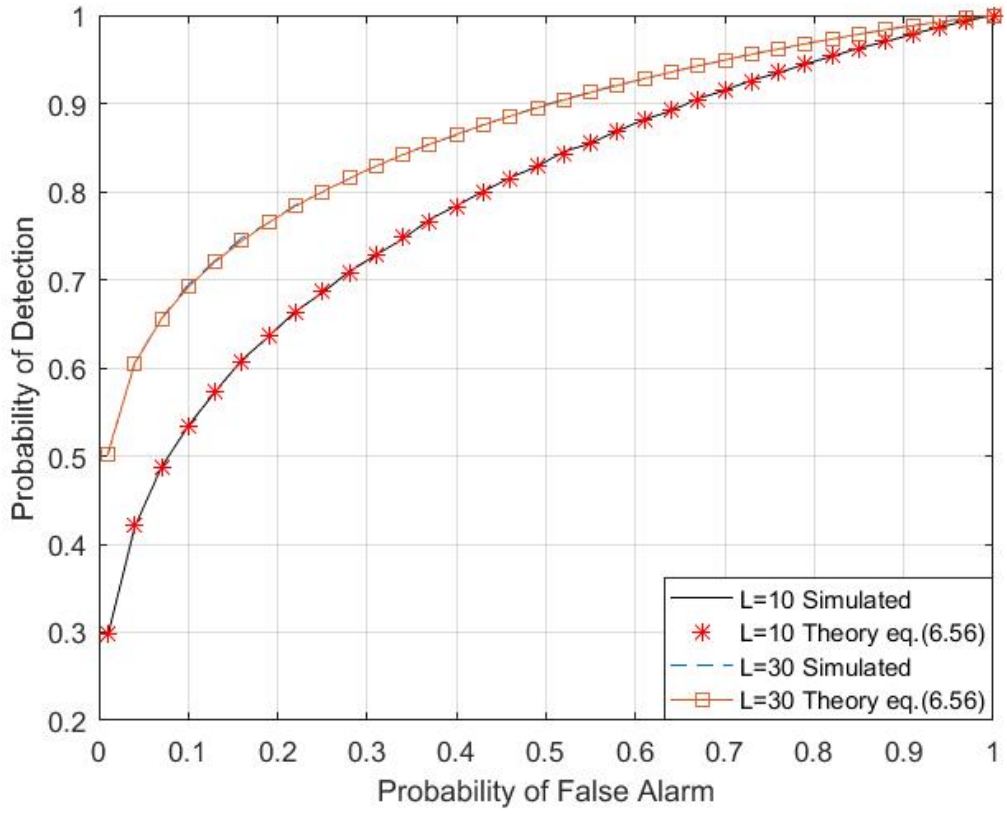

Figure 6.2: Performance of the system over Rayleigh channel.

Chapter 7

Conclusions and Future Works

In this chapter, we will summarize the main contributions of the thesis and present some ideas for the future.

7.1 Conclusions

- In chapter 1 and 2, we gave a detailed description of radar systems, power combiners, and energy detection technique. We highlight the implementation methods of radar systems. We explain the types of radar in detail. We talk about the main types of the power combiners and we present some methods of the power combiners. We explain the energy detection technique that is used to define the presence or the absence of the signal.

- In chapter 3, we showed that the efficiency of traditional power combining systems for high-power radar systems is significantly reduced in case of the failure. We proposed using the energy detection technique to provide digital control output to reduce the power loss. Also, the proposed system has a compact design and fast time response.

- In chapter 4, we showed that the traditional way for implementing the proposed band-pass filter is not efficient. Therefore, we propose using coupled structure technique to have a very compact size. We presented how we used several techniques, such as stepped transform and coupled-line resonator, to improve the performance of our proposed filter.

- In chapter 5, we presented the circuit implementation of the controlling circuit. We discussed the reasons for choosing the rms and envelope threshold detection board (ADL 5904) to apply the energy detection technique. We presented the specifications of the micro-controller (ATmega 329) and the dual full bridge driver (L298). Finally, we illustrated how the waveguide switch (WR229) is controlled electrically.

- In chapter 6, we investigated the performance of the energy detection over AWGN and Rayleigh channels. We showed that by increasing the number of samples, the performance of the energy detection improves.

7.2 Future Works

- Frequency selective surfaces can be used to decrease the insertion loss of the filter. This can be implemented using other guiding structure such as packaged microstrip line or printed ridge gap waveguide.

- The out of band rejection can be enhanced by using successive filtering stages. This way, the noise power be reduced which will enhance the overall switching sensitivity.

- The provided analysis assumes over Rayleigh channel in the system, however, the actual coupling devices can have a different effect on the fading environment. Statistical modeling for this effect can provide more accurate results for the ROC performance.

- In this work, we used energy detection, which uses the mean square value as the decision statistic. However, this work can be extended by using p-norm detectors which can provide better performance. The optimal p-norm detector and its performance can be a future work direction.

Bibliography

[1] M. I. Skolnik, "Radar Handbook," 2ed, London: McGraw-Hill Publishing Co., Dec 1989.

[2] M. M. Azer, S. I. Shams and A. M. M. A. Allam, "Compact double-sided printed omni-directional ultra wideband antenna," *IEEE Antennas and Propagation Society International Symposium,* Toronto, ON, pp. 1-4, 2010.

[3] H. H. Awadalla, S. I. Shams and A. M. M. A. Allam, "A compact, symmetric branched chain monopole for dual wide band operation," *10th Mediterranean Microwave Symposium,* Guzelyurt, pp. 56-59, 2010.

[4] M. A. A. Fattah, A. M. M. A. Allam and S. I. Shams, "Irregular pentagon monopole structured antenna for ultra-wideband communication systems," *IEEE Middle East Conference on Antennas and Propagation (MECAP),* Cairo, pp. 1-4, 2010.

[5] M. A. Issa, M. H. Sharaf, S. I. Shams and A. M. M. A. Allam, "Stair-monopole antenna and irregular pentagon antenna in ultra-wideband applications: Detailed study," *IEEE International Symposium on Antennas and Propagation (APSURSI),* Spokane, WA, pp. 1766-1769, 2011.

[6] M. Skolnik,"Introduction to Radar Systems," 2 ed. New York: McGraw Hill Book Co., 1980.

[7] C. A. Levis, J. T. Johnson, and F. L. Teixeira, *Radiowave Propagation: Physics and Applications.* Hoboken, NJ, USA: Wiley, 2010.

[8] O. H. Hassan, S. I. Shams and A. M. M. A. Allam, "Dual-band circularly polarized antenna with CPW feeding structure," *Asia-Pacific Microwave Conference,* Yokohama, pp. 2052-2055, 2010.

[9] K. S. Mohamed, S. I. Shams and A. M. M. A. Allam, "Compact inset-fed microstripline circularly polarized antenna," *IEEE Middle East Conference on Antennas and Propagation (MECAP),* Cairo, pp. 1-4, 2010.

[10] G. B. Abdelsayed, S. I. Shams and A. M. M. A. Allam, "Triple-band circularly polarized slotted patch antenna for GPS and UMTS systems," *10th Mediterranean Microwave Symposium,* Guzelyurt, pp. 448-451, 2010.

[11] M. A. Eldewiny, S. I. Shams and A. M. M. Allam, "A compact multiband planar antenna for DCS-1900/PCS/UMTS/WCDMA-2000/WLAN and WiMAX applications," *Asia-Pacific Microwave Conference,* Yokohama, pp. 2060-2063, 2010.

[12] Grebennikov, Andrei, "Power combiners, impedance transformers and directional couplers: part I." *High Frequency Electronics.* vol. 6, pp. 20-38 December 2007.

[13] S. I. Shams and A. A. Kishk, "Design of 3-dB Hybrid Coupler Based on RGW Technology," in *IEEE Transactions on Microwave Theory and Techniques,* vol. 65, no. 10, pp. 3849-3855, Oct. 2017.

[14] M. M. M. Ali, S. I. Shams and A. R. Sebak, "Printed Ridge Gap Waveguide 3-dB Coupler: Analy and Design Procedure," in *IEEE Access,* vol. 6, pp. 8501-8509, 2018.

[15] S. I. Shams and A. A. Kishk, "Wide band power divider based on Ridge gap waveguide," *17th International Symposium on Antenna Technology and Applied Electromagnetics (ANTEM),* Montreal, QC, pp. 1-2, 2016.

[16] Sean C. Ortiz, "High Power Spatial Combiners: Tile and Tray Approaches," North Carolina State University, Department of Electrical Engineering, Raleigh, NC, 27695, 2001.

[17] S. I. Shams, M. A. Abdelaal and A. A. Kishk, "SIW magic tee fed by printed Ridge Gap Waveguide design," *17th International Symposium on Antenna Technology and Applied Electromagnetics (ANTEM),* Montreal, QC, pp. 1-2, 2016.

[18] N. Hoven. "On the Feasibility of Cognitive Radio", Master's the University of California at Berkeley. Berkeley CA, 2005.

[19] R. Sindhubargavi, M. Yuvasrri Sindhu and R. Saravanan, "Spectrum Sensing using Energy Detection Technique for Cognitive Radio Networks using PCA Technique,"

Sastra University, *Indian Journal of Science and Technology,* vol 7, no. 4, pp. 40–45, April 2014.

[20] Robert E. Collin, Foundations for Microwave Engineering, 2ed, Wiley-IEEE Press 2000.

[21] G. Galati and P. van Genderen, "History of radar: The need for further analy and disclosure," *11th European Radar Conference,* Rome, pp. 25-28, 2014.

[22] M. Guarnieri, "The Early History of Radar [Historical]," in *IEEE Industrial Electronics Magazine,* vol. 4, no. 3, pp. 36-42, Sept. 2010.

[23] V. S. Chernyak and I. Y. Immoreev, "A Brief History of Radar," in *IEEE Aerospace and Electronic Systems Magazine,* vol. 24, no. 9, pp. B1-B32, Sept. 2009.

[24] Niraj Prasad Bhatta and M. GeethaPriya,"RADAR and its Applications," *International Science Press,* IJCTA, 10(03), pp. 1-9, 2017.

[25] Tarun Agarwal. "RADAR-Basics, Types & Applications," Retrieved from https://www.elprocus.com/radar-basics-types-and-applications/. Accessed on April 27, 2018.

[26] Lav Varshney. "Radar system components and system design," *Technical report,* Syracuse Research Corporation 6225 Running Ridge Road North Syracuse, NY 13212-2509, November 2002.

[27] S. Pisa, E. Pittella and E. Piuzzi, "A survey of radar systems for medical applications," in *IEEE Aerospace and Electronic Systems Magazine,* vol. 31, no. 11, pp. 64-81, November 2016.

[28] C. M. Alabaster, "Suppression of co-channel interference in high duty ratio pulsed radar receivers," *International Conference on Radar Systems (Radar),* Belfast, pp. 1-6, 2017.

[29] Ferran Martiacuten; Lei Zhu; Jiasheng Hong; Francisco Medina, "BALANCED POWER DIVIDERS/COMBINERS," in *Balanced Microwave Filters,* 1, Wiley-IEEE Press, 2018.

[30] R. A. Beltran, “High-efficiency and flat-gain Doherty type transmitter using a 180-degree hybrid-combiner,” *IEEE MTT-S International Microwave Symposium (IMS),* Honololu, HI, pp. 1726-1729, 2017.

[31] T. H. Wang and J. H. Chen, “Power recycling using Wilkinson power combiner with pulsewidth modulation,” *IEEE International Symposium on Radio-Frequency Integration Technology (RFIT),* Seoul, pp. 223-225, 2017.

[32] U. H. Gysel, “A New N-Way Power Divider/Combiner Suitable for High-Power Applications,” *IEEE-MTT-S International Microwave Symposium,* Palo Alton, CA, pp. 116-118, 1975.

[33] IDA KLÄPPEVIK, “Analy, Construction and Evaluation of a Radial Power Divider/Combiner,” Chalmers University of Technology, Department of Microtechnology and Nanoscience, Sweden 2017.

[34] K. J. Russel, “Microwave power combining techniques,” *IEEE Trans. Microwave Theory and Techs.,* vol. 27, pp. 472–478, 1979.

[35] K. Chang and C. Sun, “Millimeter-wave power-combining techniques,” *IEEE Trans. Microwave Theory and Techs.,* vol. 31, pp. 91–107, 1983.

[36] E. J. Wilkinson, “An N-way hybrid power divider,” *IRE Trans. Microwave Theory and Techs.,* vol. 8, pp. 116–118, 1960.

[37] R. Faraji-Dana and H. Javadi-Bakhsh, “A Wideband Twenty-Element Microwave Spatial Power Combiner,” *Scientia Iranica.Transaction D, Computer Science Engineering, Electrical D,* vol. 21, no. 3, pp. 853-860, 2014.

[38] P. F. Goldsmith, “Quasioptical systems: gaussian beam quasioptical propagation and applications.” *IEEE Press,* 1st ed., 1998.

[39] Orbitfr. “Radial Power Combiners,” Retrieved from http://www.orbitfr.com/sites/www.orbitfr.com/files/power-combiners-bd.pdf. Accessed on March 28, 2018.

[40] A. E. Fathy, Sung-Woo Lee and D. Kalokitis, “A simplified design approach for radial power combiners," in IEEE Transactions on Microwave Theory and Techniques, vol. 54, no. 1, pp. 247-255, Jan. 2006.

[41] M. Subhedar and G. Birajdar, “Spectrum Sensing Techniques in Cognitive Radio Networks: A Survey.” *International Journal of Next-Generation Networks (IJNGN),* vol. 3, no. 2, pp. 37–51, June 2011.

[42] M. Elsaadany and W. Hamouda, “Antenna Selection for Dual-hop Cognitive Radio Networks: A Multiple-Relay Scenario", IEEE Transactions on Vehicular Technology, vol. 66, no. 8, pp. 6754-6763, Aug. 2017.

[43] M. Elsaadany, “Optimal power allocation in cognitive networks using non-orthogonal AF relays," 39th Annual IEEE Conference on Local Computer Networks (LCN), Edmonton, AB, 2014, pp. 410-413.

[44] M. Elsaadany and T. Khattab, “Performance analysis of general order selection in decentralized cognitive radio networks," 2014 IEEE Wireless Communications and Networking Conference (WCNC), Istanbul, 2014, pp. 1827-1831.

[45] P. Pawełczak, “Cognitive Radio: Ten Years of Experimentation and Development,” *IEEE Communications Magazine,* vol. 49, no. 3, pp. 90-100, Mar. 2011.

[46] I. F. Akyildiz, Won-Yeol Lee, M. C. Vuran, and Sh. Mohanty, “NeXt generation/dynamic spectrum access/cognitive radio wireless networks: A survey,” *Computer Networks,* vol. 50, no. 13, pp. 2127-2159, 2006.

[47] M. Elsaadany and W. Hamouda, “Performance Analysis of Non-Orthogonal AF Relaying in Cognitive Radio Networks," in IEEE Wireless Communications Letters, vol. 4, no. 4, pp. 373-376, Aug. 2015.

[48] I. F. Akyildiz, B. F. Lo, and R. Balakrishnan, “Cooperative spectrum sensing in cognitive radio networks: A survey,” *Physical Communication,* vol. 4 no. 1 pp. 40-62, 2011.

[49] M. Elsaadany and W. Hamouda, “Energy Efficient Design for Non-Orthogonal AF Relaying in Underlay Spectrum Sharing Networks", IEEE International Conference on Communications (ICC), 2016.

[50] M. Elsaadany and W. Hamouda, “Enhancing the Performance of Amplify-and-Forward Cognitive Relay Networks: A Multiple-Relay Scenario", IEEE Global Communications Conference (GLOBECOM), 2015.

[51] A. Garhwal, and P. P. Bhattacharya "A Survey on Dynamic Spectrum Access Techniques for Cognitive Radio," *International Journal of Next-Generation Networks,* vol. 3, no. 4, pp. 15-32, 2012.

[52] S. Ziafat, W. Ejaz, and H. Jamal, "Spectrum sensing techniques for cognitive radio networks: Performance analy," *IEEE MTT-S International Microwave Workshop Series on Intelligent Radio for Future Personal Terminals,* pp. 1-4, 2011.

[53] C. S. Rawat, G. G. Korde, "Comparison between Energy Detection and Cyclostationary Detection for Transmitter Section of Cognitive Radio," *International Journal Of Electrical, Electronics And Data Communication,* Vol. 3, no. 12, Dec. 2015.

[54] D. Cabric, S. M. Mishra, and R. W. Brodersen, "Implementation issues in spectrum sensing for cognitive radios," *in Proceedings of the 38th Asilomar Conference on Signals, Systems and Computers,* vol. 1, pp. 772–776, Nov. 2004.

[55] David M. Pozar "Microwave Engineering," John Wiley & Sons, 3ed, 2005.

[56] M. Stănculescu, L. Iordache, M. Iordache, D. Niculae and V. Bucată, "Using S parameters in wireless power transfer analy," *10th International Symposium on Advanced Topics in Electrical Engineering (ATEE),* Bucharest, pp. 107-112, 2017.

[57] Pozar, David. "Microwave Engineering," 2ed, August 1997.

[58] T. Djeddi, M. Elsaadany, S. I. Shams and W. Hamouda, "Compact Ultra-Wideband Printed Bandpass Filter Based on Coupled-Line Resonator Loading," *17th International Symposium on Antenna Technology and Applied Electromagnetics (ANTEM),* Watreloo, ON, pp. 1-2, 2018.

[59] S. I. Shams and A. A. Kishk, "Printed Texture With Triangle Flat Pins for Bandwidth Enhancement of the Ridge Gap Waveguide," in *IEEE Transactions on Microwave Theory and Techniques,* vol. 65, no. 6, pp. 2093-2100, June 2017.

[60] S. I. Shams and A. A. Kishk, "Wideband Coaxial to Ridge Gap Waveguide Transition," in *IEEE Transactions on Microwave Theory and Techniques,* vol. 64, no. 12, pp. 4117-4125, Dec. 2016.

[61] S. I. Shams and A. A. Kishk, "Determining the Stopband of a Periodic Bed of Nails From the Dispersion Relation Measurements Prediction," in *IEEE Transactions on*

Components, Packaging and Manufacturing Technology, vol. 7, no. 4, pp. 621-629, April 2017.

[62] S. I. Shams and A. A. Kishk, "Double cone ultra wide band unit cell in ridge gap waveguides," in *IEEE Antennas and Propagation Society International Symposium (APSURSI),* Memphis, TN, pp. 1768-1769. 2014.

[63] S. I. Shams and A. A. Kishk, "Ridge gap waveguide to microstrip line transition with perforated substrate," *USNC-URSI Radio Science Meeting (Joint with AP-S Symposium),* Memphis, TN, 2014, pp. 215-215. 2014.

[64] Analog Devices. "Envelope and TruPwr RMS Detector," Retrieved from http://www.analog.com/media/en/technical-documentation/data-sheets/ADL5511.pdf. Accessed on January 16, 2018.

[65] Analog Devices. "Envelope Threshold Detector/Trigger," Retrieved from http://www.analog.com/media/en/technical-documentation/data-sheets/ADL5910.pdf. Accessed on January 16, 2018.

[66] Analog Devices. "Detector with Envelope Threshold Detection," Retrieved from http://www.analog.com/media/en/technical-documentation/data-sheets/ADL5904.pdf. Accessed on January 16, 2018.

[67] ATmel. "8-bit AVR Microcontroller with 4/8/16/32K Bytes In-System Programmable Flash," Retrieved from https://www.mouser.com/pdfdocs/Gravitech-ATMEGA328-datasheet.pdf. Accessed on May 1, 2018.

[68] SparkFun Electronics. "Dual Fill-bridge Driver," Retrieved from https://www.sparkfun.com/datasheets/Robotics/L298-H-Bridge.pdf. Accessed on May 1, 2018.

[69] RF Com. "Waveguide Switches," Retrieved from http://www.rfcom.co.uk/upfiles/siv-waveguide-switches.pdf. Accessed on March 1, 2018.

[70] Advanced Switch Technology. "Switches," Retrieved from https://docs.wixstatic.com/ugd/397bbf-3132dd99ea0d483890b8bab63993b10e.pdf. Accessed on March 3, 2018.

[71] H. Urkowitz,"Energy detection of unknown deterministic signals," *Proc. IEEE,* vol. 55, pp. 523–531, April 1967.

[72] C. E. Shannon, "Communication in the presence of noise," *Proc. IRE,* vol. 37, pp. 10–21, January 1949.

[73] Davenport, Wilbur B., and William L. Root. Random Signals and Noise. New York: McGraw-Hill, 1958.

[74] M. Zelen and N. C. Severo, "Probability functions," in *Handbook of Mathematical Functions,* M. Abramovitz and J. A. Stegun, Eds., NBS Applied Math. Series 55. Washington, DC: U. S. Government Printing Office, vol. 55, 1964.

[75] R. A. Fisher and F. Yates, *Statistical Tables for Biological, Agriculture, and Medical Research.* Edinburgh, U.K.: Oliver and Boyd, 1938.

[76] A. Hald, Statistical Tables and Formulas. New York: Wiley, 1952.

[77] P. B. Patnaik, "The noncentral x^2 and F distributions and their applications," *Biometrika*, vol. 36, pp. 202-232, 1949.

[78] E. Fix, "Tables of Noncentral x^2," *Publications in Statistics.* Berkeley, CaIif.: University of California Press, vol. 1, no. 2, pp. 15-19, 1949.

[79] F. F. Digham et al., "On the Energy Detection of Unknown Signals over Fading Channels," in Proceedings of the *IEEE International Conference on Communication,* Seattle, Washington, USA, pp. 3575-3579, 2003.

[80] I. S. Gradshteyn and I. M. Ryzhik, Table of Integrals, Series, and Products. San Diego, CA: Academic Press, sixth ed., 2000.

[81] J. G. Proakis, Digital Communications. McGraw-Hill, fourth ed., 2001.

[82] A. H. Nuttall, "Some integrals involving the QM-function," *Naval Underwater Systems Center (NUSC) technical report,* May 1974.

[83] H. V. Trees, Detection, Estimation, and Modulation Theory. New York, NY: John Wiley & Sons, 1968.

[84] V. I. Kostylev, "Energy detection of a signal with random amplitude," in Proc. *IEEE Int. Conf. on Commun.* (ICC'02), New York City, New York, pp. 1606–1610, May 2002.